A&A 625, A126 (2019)
https://doi.org/10.1051/0004-6361/201834969
© ESO 2019

Astronomy & Astrophysics

The HADES RV programme with HARPS-N at TNG

XI. GJ 685 b: a warm super-Earth around an active M dwarf⋆

M. Pinamonti[1], A. Sozzetti[1], P. Giacobbe[1], M. Damasso[1], G. Scandariato[2], M. Perger[3,4], J. I. González Hernández[5,6], A. F. Lanza[2], J. Maldonado[7], G. Micela[7], A. Suárez Mascareño[5,8], B. Toledo-Padrón[5,6], L. Affer[7], S. Benatti[9], A. Bignamini[10], A. S. Bonomo[1], R. Claudi[9], R. Cosentino[2,11], S. Desidera[9], A. Maggio[7], A. Martinez Fiorenzano[11], I. Pagano[2], G. Piotto[9,12], M. Rainer[13], R. Rebolo[5,6], and I. Ribas[3,4]

[1] INAF – Osservatorio Astrofisico di Torino, Via Osservatorio 20, 10025 Pino Torinese, Italy
e-mail: matteo.pinamonti@inaf.it
[2] INAF – Osservatorio Astrofisico di Catania, Via S. Sofia 78, 95123 Catania, Italy
[3] Institut de Ciències de l'Espai (ICE, CSIC), Campus UAB, C/ de Can Magrans s/n, 08193 Cerdanyola del Vallès, Spain
[4] Institut d'Estudis Espacials de Catalunya (IEEC), C/ Gran Capità 2-4, 08034 Barcelona, Spain
[5] Instituto de Astrofísica de Canarias (IAC), 38205 La Laguna, Tenerife, Spain
[6] Universidad de La Laguna, Departamento Astrofísica, 38206 La Laguna, Tenerife, Spain
[7] INAF – Osservatorio Astronomico di Palermo, piazza del Parlamento 1, 90134 Palermo, Italy
[8] Observatoire Astronomique de l'Université de Genéve, 1290 Versoix, Switzerland
[9] INAF – Osservatorio Astronomico di Padova, vicolo dell'Osservatorio 5, 35122 Padova, Italy
[10] INAF – Osservatorio Astronomico di Trieste, Via G. B. Tiepolo 11, 34143 Trieste, Italy
[11] Fundación Galileo Galilei – INAF, Ramble José Ana Fernandez Pérez 7, 38712 Breña Baja, TF, Spain
[12] Dipartimento di Fisica e Astronomia, Università di Padova, Via Marzolo 8, 35131 Padova, Italy
[13] INAF – Osservatorio Astrofisico di Arcetri, Largo E. Fermi 5, 50125 Firenze, Italy

Received 22 December 2018 / Accepted 26 March 2019

ABSTRACT

Context. Small rocky planets seem to be very abundant around low-mass M-type stars. Their actual planetary population is however not yet precisely understood. Currently, several surveys aim to expand the statistics with intensive detection campaigns, both photometric and spectroscopic.

Aims. The HADES program aims to improve the current statistics through the in-depth analysis of accurate radial-velocity (RV) monitoring in a narrow range of spectral sub-types, with the precision needed to detect small planets with a few Earth masses.

Methods. We analyse 106 spectroscopic HARPS-N observations of the active M0-type star GJ 685 taken over the past five years. We combine these data with photometric measurements from different observatories to accurately model the stellar rotation and disentangle its signals from genuine Doppler planetary signals in the RV data. We run an MCMC analysis on the RV and activity index time series to model the planetary and stellar signals present in the data, applying Gaussian Process regression technique to deal with the stellar activity signals.

Results. We identify three periodic signals in the RV time series, with periods of 9, 24, and 18 d. Combining the analyses of the photometry of the star with the activity indexes derived from the HARPS-N spectra, we identify the 18 d and 9 d signals as activity-related, corresponding to the stellar rotation period and its first harmonic, respectively. The 24 d signal shows no relation to any activity proxy, and therefore we identify it as a genuine planetary signal. We find the best-fit model describing the Doppler signal of the newly found planet, GJ 685 b, corresponding to an orbital period $P_b = 24.160^{+0.061}_{-0.047}$ d and a minimum mass $M_P \sin i = 9.0^{+1.7}_{-1.8}$ $M_\oplus$. We also study a sample of 70 RV-detected M-dwarf planets, and present new statistical evidence of a difference in mass distribution between the populations of single- and multi-planet systems, which can shed new light on the formation mechanisms of low-mass planets around late-type stars.

Key words. techniques: radial velocities – stars: individual: GJ 685 – stars: activity – instrumentation: spectrographs – planets and satellites: detection

1. Introduction

Most of the early surveys hunting for exoplanets, which employed the radial-velocity (RV) method, directed their efforts towards dwarf stars of spectral type G or K, usually in a range around the mass of the Sun (e.g. Queloz et al. 2001; Valenti & Fischer 2005; Tamuz et al. 2008). Instead, in recent years M dwarfs have become the most promising targets for the hunt for low-mass rocky planets (e.g. Bonfils et al. 2013; Dressing & Charbonneau 2013; Sozzetti et al. 2013; Astudillo-Defru et al. 2017a) due to their more advantageous mass and radius ratios compared to solar-type stars. Moreover, with the availability of high-precision spectrographs mounted on 4 m-class telescopes, led by HARPS at La Silla (Northern High Accuracy Radial velocity Planet Searcher, Mayor et al. 2003)

⋆ Based on observations made with the Italian Telescopio Nazionale *Galileo* (TNG), operated on the island of La Palma by the INAF – Fundación Galileo Galilei at the Roche de Los Muchachos Observatory of the Instituto de Astrofísica de Canarias (IAC); photometric observations made with the APACHE array located at the Astronomical Observatory of the Aosta Valley; photometric observations made with the robotic telescope APT2 (within the EXORAP programme) located at Serra La Nave on Mt. Etna.

and recently backed up by its younger twin HARPS-N at TNG (Cosentino et al. 2012), it was possible to reach 1 m s^{-1} precision allowing the detection of small Earth-like rocky planets (e.g. Anglada-Escudé et al. 2016a; Astudillo-Defru et al. 2017b).

It is becoming clear that giant gas planets are less frequent around low-mass stars than around those of solar type, as expected from theoretical studies (e.g. Laughlin et al. 2004; Mordasini et al. 2009), while low-mass rocky planets are proving to be much more common around low-mass stars, both in RVs (e.g. Tuomi et al. 2014, and references therein) and transit (e.g. Gaidos et al. 2016, and references therein) observations. Nevertheless, the complete characterization of this abundant population of rocky planets around M dwarfs is hindered by the strong effects of the photospheric and magnetic activity of the latter, which can produce RV signals as large as tens of meters per second. This can result in stellar signals being mistaken for planetary signals or otherwise uncertain results for systems around active stars (e.g. Bonfils et al. 2007; Baluev 2013a; Robertson et al. 2014), and also around quieter targets, which can still present periodic signals of unclear nature (e.g. Robertson et al. 2015; Anglada-Escudé et al. 2016b).

The Harps-n red Dwarf Exoplanet Survey (HADES) programme is a collaboration between the Italian Global Architecture of Planetary Systems (GAPS, Covino et al. 2013; Desidera et al. 2013; Poretti et al. 2016) Consortium[1], the Institut de Ciències de l'Espai de Catalunya (ICE), and the Instituto de Astrofísica de Canarias (IAC). The aim of the survey is to characterise the exoplanetary systems around a well-defined sample of M dwarfs, with spectral type between dM0 and dM3. High-precision RVs of the sample have been collected over the course of five years with the HARPS-N at TNG spectrograph. Several planets have been discovered as part of the survey (e.g. Affer et al. 2016; Suárez Mascareño et al. 2017; Perger et al. 2017a; Pinamonti et al. 2018), and also some more general studies have already been performed on the samples, studying both the stellar properties (Maldonado et al. 2017; Scandariato et al. 2017; Suárez Mascareño et al. 2018; González-Álvarez et al. 2019) and the preliminary planetary population statistics (Perger et al. 2017b). Moreover, a collaboration between the HADES and CARMENES programs resulted in the detection of the super-Earth Gl 49 b (Perger et al. 2019).

In this work we present the search for planetary companions around the M dwarf GJ 685, based on high-precision spectroscopic observations carried out with HARPS-N as part of the HADES programme. We also take advantage of ancillary photometric observations of the target to better constrain the stellar activity signal in the RVs.

In Sect. 2 we describe the Doppler measurements of GJ 685 collected for this analysis, and in Sect. 3 we briefly discuss the physical properties of the host star. The independent analyses of two photometric datasets are presented in Sect. 4. We describe our periodogram analyses of the RV data and stellar activity indexes in Sect. 5. We proceed to find the best-fit parameters for the models describing the activity and RV time series via a Monte Carlo Markov chain (MCMC) analysis in Sect. 6. Finally, we summarise and discuss our findings in the more general context of the current population of M-dwarf RV-detected planetary systems in Sect. 7.

[1] http://www.oact.inaf.it/exoit/EXO-IT/Projects/Entries/2011/12/27_GAPS.html

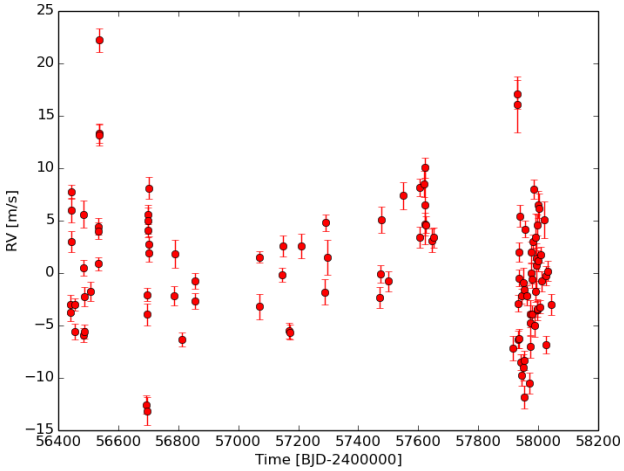

Fig. 1. HARPS-N RV time series of GJ 685.

2. Spectroscopic observations

As part of the HADES RV programme, GJ 685 has been observed from BJD = 2 456 439.6 (27 May 2013) to BJD = 2 458 044.4 (17 October 2017) with the HARPS-N spectrograph, connected by fibres to the Nasmyth B focus through a Front End Unit of the 3.58 m Telescopio Nazionale *Galileo* (TNG) in La Palma, Spain. HARPS-N is a fibre-fed, cross-dispersed echelle spectrograph with a spectral resolution of 115 000, covering a wavelength range from 3830 to 6900 Å. We observed with fixed integration times of 900 s to obtain data of sufficient signal-to-noise ratio ($S/N > 20$) and to average out short-term periodic oscillations of the star, such as p-modes (Dumusque et al. 2011).

The total number of data points acquired was 106 over a time span of 1605 days. The time series is shown in Fig. 1. The observations were gathered without the simultaneous Th-Ar calibration, which could contaminate the Ca II H and K lines due to the long exposure times and the relative faintness of M-dwarf targets in the blue part of the spectra. Moreover, these lines are crucial in the analysis of stellar activity (e.g. Giampapa et al. 1989; Forveille et al. 2009), which is particularly important for active late-type stars. A precise acquisition of the Ca II H and K lines was therefore preferred over a better correction of possible instrumental drifts. Perger et al. (2017b) used other GAPS target spectra gathered by the Italian team on the same nights using the simultaneous Th-Ar calibration to quantify this effect, and found a mean inter-night instrumental drift of the order of 1 m s^{-1} over the whole HADES sample. Nevertheless, for some of the brightest targets of the sample, some spectra could be safely taken with the simultaneous drift calibrations without problems for the Ca II H and K observations (Perger et al. 2017a). This helped us to monitor the instrumental drift over the single target: for GJ 685, four spectra were collected with the simultaneous Th-Ar calibrations, measuring a mean inter-night instrumental drift of ∼0.5 m s^{-1}. Any residual drift in the time series was taken into account in our final model as discussed in Sect. 6.2.

The data reduction and the RV extraction were performed using the HARPS-N Data Reduction Software (DRS, Lovis & Pepe 2007) and the TERRA pipeline (Template-Enhanced Radial velocity Re-analysis Application, Anglada-Escudé & Butler 2012), respectively. The latter is considered to be more accurate when applied to M-dwarfs, with respect to the DRS. For a more thorough discussion of the DRS and TERRA performances on the HADES targets see Perger et al. (2017b).

Table 1. Stellar parameters for the target GJ 685.

Parameter	GJ 685
Spectral type	M0.5 [(a)]
$T_{\rm eff}$ (K)	3816 ± 69 [(a)]
[Fe/H] (dex)	-0.15 ± 0.09 [(a)]
Mass ($M_\odot$)	0.55 ± 0.06 [(a)]
Radius ($R_\odot$)	0.54 ± 0.05 [(a)]
$\log g$ (cgs)	4.72 ± 0.05 [(a)]
$\log L_*/L_\odot$	-1.253 ± 0.094 [(a)]
$v \sin i$ (km s^{-1})	1.33 ± 0.42 [(a)]
$\log R'_{\rm HK}$	-4.79 ± 0.04 [(b)]
$P_{\rm rot}$	16.3 ± 4.2 [(b)]
α (J2000)	$17^{\rm h}:35^{\rm m}:35.0^{\rm s}$ [(c)]
δ (J2000)	$+61^\circ:40':45.6''$ [(c)]
$B - V$ (mag)	1.48
V (mag)	9.97
J (mag)	6.884 [(d)]
H (mag)	6.271 [(d)]
K (mag)	6.066 [(d)]
π (mas)	69.825 ± 0.039 [(c)]
μ_α (mas yr^{-1})	261.895 ± 0.055 [(c)]
μ_δ (mas yr^{-1})	-514.400 ± 0.063 [(c)]

References. [(a)]Maldonado et al. (2017); [(b)]Suárez Mascareño et al. (2018); [(c)]Gaia Collaboration (2018); [(d)]Cutri et al. (2003).

The mean internal error of the TERRA data is 1.02 m s^{-1}, with a few low-S/N data with $\sigma_{\rm RV} > 2.0$ m s^{-1}. With an rms of 6.16 m s^{-1}, GJ 685 is one of the HADES targets with the largest RV dispersion. The TERRA pipeline also corrected the RV data for the perspective acceleration of GJ 685, $\mathrm{d}v_r/\mathrm{d}t = 0.11$ m s^{-1} yr^{-1}.

3. Stellar properties of GJ 685

The star GJ 685 is a high proper motion nearby ($\pi = 69.825 \pm 0.039$ mas) M0-type dwarf. We used the stellar parameters published by Maldonado et al. (2017), which were calculated applying the empirical relations by Maldonado et al. (2015) to the same HARPS-N spectra from which we derived the RV time series. The parallax and proper motions of the star were taken from the *Gaia* Data Release 2 (Gaia Collaboration 2018). All the stellar parameters of GJ 685 are listed in Table 1.

Suárez Mascareño et al. (2018) studied the presence of signatures of magnetic cycles and rotation on the stars of the HADES sample, measuring the rotation periods and $\log R'_{\rm HK}$ for several stars of the sample[2]. For GJ 685, Suárez Mascareño et al. (2018) derived, from the variability in the S-index and Hα activity indexes and RV time series, a rotation period of 16.3 ± 4.2 d finding no evidence for the presence of a magnetic cycle. The rotation period value is listed in Table 1 along with the measured value of $\log R'_{\rm HK}$.

4. Photometric monitoring

As with most of the targets of the HADES sample, GJ 685 has been monitored photometrically by means of the APACHE (Sozzetti et al. 2013) and EXORAP (EXOplanetary systems Robotic APT2 Photometry) surveys. The two surveys perform regular follow-up observations of HADES M-dwarf targets to constrain the stellar rotation periods by analysing the photometric variability. We briefly discuss the analyses of the datasets collected by the two surveys in the following sections.

4.1. APACHE photometry

GJ 685 was monitored for 64 nights between BJD = 2 456 456.4 (12 Jun 2013) and BJD = 2 456 793.6 (15 May 2014) with one of the five 40 cm telescopes composing the APACHE array located at the Astronomical Observatory of the Autonomous Region of the Aosta Valley (OAVdA, +45.7895 N, +7.478 E, 1650 m.a.s.l.). The observations were collected following the standard APACHE procedure, and the images were reduced with the standard pipeline TEEPEE by the APACHE team (Giacobbe et al. 2012).

Since Suárez Mascareño et al. (2018) calculated the rotation period of GJ 685 to be $P_{\rm rot} = 16.3 \pm 4.2$ d, we performed Generalized Lomb Scargle periodogram analysis (GLS, Zechmeister & Kürster 2009) of the photometric data, looking for similar periodicities. To do so we binned the data over each night to average out the short-period noise due to the high number of very close data points. This resulted in a time series of 64 data points over a time span of 337 d, with an rms of 0.012 mag.

The results of the GLS analysis, which covered periods between 1 d and the time span of the time series, are shown in Fig. 2, with the highest peak at a period of $P_{\rm rot,\,AP} = 16.85 \pm 0.12$ d with a theoretical false alarm probability (FAP) of 1.9%, in good agreement with the rotation period found by Suárez Mascareño et al. (2018). It is also worth noticing that there is no significant peak at longer periods.

4.2. EXORAP photometry

In the framework of the EXORAP project, we observed GJ 685 using an 80 cm f/8 Ritchey-Chretien robotic telescope (APT2) located at Serra la Nave on the Mt. Etna and operated by the INAF-Catania Astrophysical Observatory. We collected approximately 200 measurements in each band between 5 May 2014 and 6 Sept 2017. Data reduction was preformed with overscan, bias, dark subtraction, and flat fielding with IRAF procedures and visually inspected to check the data quality (see Affer et al. 2016 for details).

The scatter of the B and V photometry is slightly larger than 0.01 mag, which corresponds to the intra-night sensitivity of the survey. This suggests that there is some jitter of stellar origin in the collected data. The pooled variance (PV) analysis (Scandariato et al. 2017, and references therein) identifies a significant timescale around 20 d, but the precision of the PV technique is not sufficient to distinguish the 18 and 24 d periodicities that we discuss in Sect. 5.1. The GLS periodogram analysis shows a low-significance peak again around 20 d, while the GP analysis converges directly to an 18 d period, excluding longer periods closer to 24 d.

The analysis of the RI photometry does not lead to any significant result, as the scatter of the data of ~0.01 mag is dominated by the inter-night sensitivity of the survey. This is consistent with a scenario where the photometric scatter is dominated by cool photospheric spots, whose contrast against the unspotted photosphere is larger in the bluer bands than in R and I. This is also consistent with other similar analyses we published in other papers of the HADES series.

[2] Suárez Mascareño et al. (2018) extended the definition of $\log R'_{\rm HK}$ for application on M-dwarfs spectra, following a procedure very similar to the one used by Astudillo-Defru et al. (2017c).

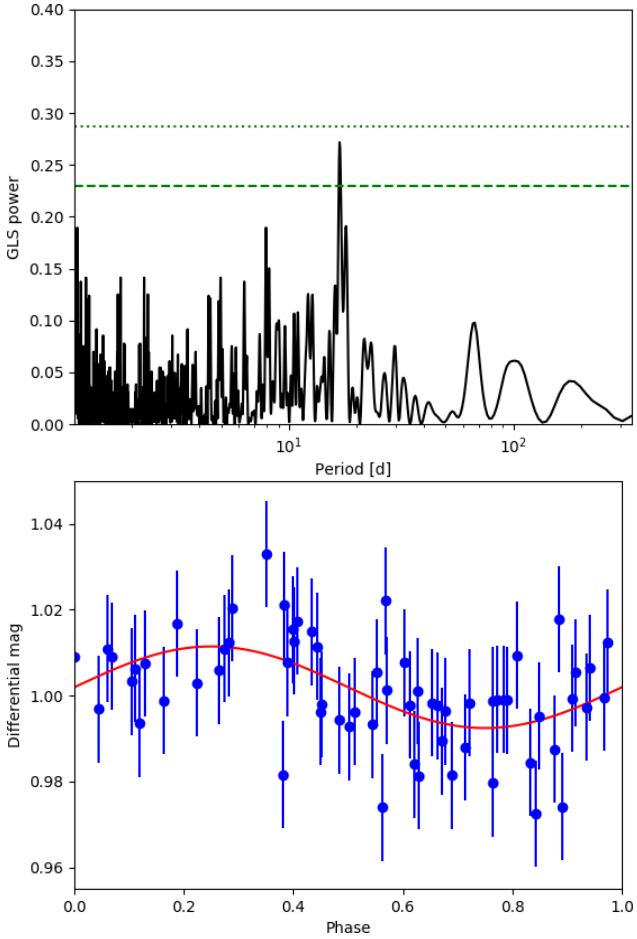

Fig. 2. *Upper panel*: GLS periodograms of the APACHE photometric data. The dotted and dashed horizontal lines indicate the 1 and 10% FAP levels, respectively. *Lower panel*: APACHE light curve phase-folded over the 16.85 d period found by the GLS periodogram. The red line represents the best-fit model.

5. Periodogram analyses

We started by analysing our spectroscopic data by means of GLS periodograms in order to identify significant periodicities in our time series, and compare the signals identified in the RV and activity indexes time series to pinpoint activity-related signals in the RV time series.

5.1. Radial velocity periodograms

First we analysed the RV time series, identifying additional significant periodicities by pre-whitening until no significant signal was found in the GLS periodogram below the FAP = 10% level. We computed the GLS FAPs via bootstrap randomisation with 10 000 iterations (Endl et al. 2001). The resulting periodograms are shown in Fig. 3. The strongest peak in the first periodogram is at $P = 9$ d, which is probably due to stellar activity, being roughly half the rotation period of the star $P_{\rm rot} = 16.3 \pm 4.2$ d, as derived by Suárez Mascareño et al. (2018) and confirmed by our photometric analysis in the previous section. After subtracting this signal we see that a peak around $P = 23.66$ d rises from the periodogram, along with a clustered peak around $P = 18$ d. The latter can be related again to the activity signal of the star, proving that a simple sinusoidal fit with $P = P_{1/2} = 9$ d is not sufficient to model the influence of active regions on the RVs. We thus identify $P_{\rm rot} = 18$ d as the rotation period of the star. It is worth noting that this rotation period is longer than the one derived from the analysis of the APACHE photometry in Sect. 4.1. This can be explained as a consequence of two effects: firstly, activity signals in the photometry can differ from those present in the RV time series, depending on the nature of the active regions present on the star (e.g. Kürster et al. 2003; Dumusque et al. 2014); secondly, the rotation signal is relatively weak in the photometry,

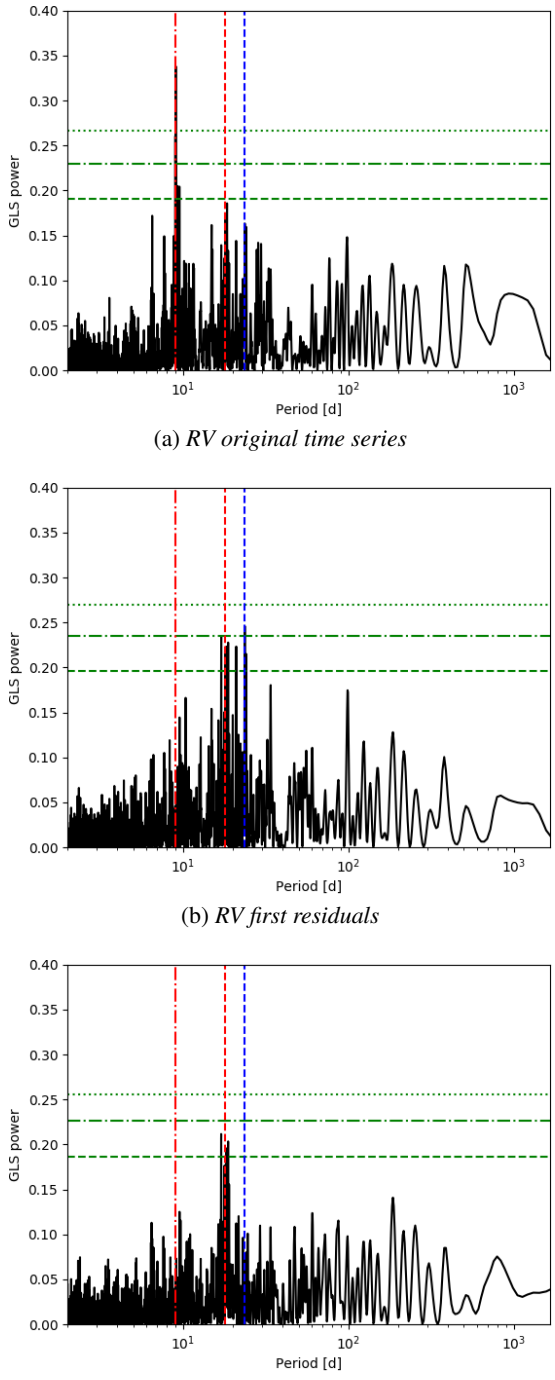

(a) *RV original time series*

(b) *RV first residuals*

(c) *RV second residuals*

Fig. 3. GLS periodograms of the RV time series and residuals after consecutive signal fits. The red vertical lines indicate the potential rotation period (dashed) and its first harmonic (dot-dashed), while the dashed blue vertical lines marks the orbital period of the planetary candidate. The dotted, dash-dotted, and dashed horizontal lines indicate the 0.1, 1, and 10% FAP levels, respectively.

with a theoretical FAP > 1% in the APACHE analysis and not appearing clearly in the EXORAP datasets, and thus a relatively large uncertainty in the rotation period is not surprising. It is also worth noting that a peak at $P = 18$ d is indeed present in the periodogram in Fig. 2, even if weaker than the main peak. The $P = 23.7$ d signal instead does not appear to be easily related to the assumed rotation period of the star or its harmonics, and it is also relatively strong in the periodogram (FAP = 0.47%). We therefore suspect it to be a genuine Keplerian Doppler shift due to an orbiting planet, hereafter GJ 685 b. The semi-amplitude of the signal at $P = 23.661 \pm 0.037$ d identified in the periodogram is $K = 3.11 \pm 0.53$ m s^{-1}.

For a more comprehensive view of the periodicities present in the RV data, we also studied the time series with the Bayesian Generalized Lomb-Scargle (BGLS, Mortier et al. 2015) and FREquency DEComposer (FREDEC, Baluev 2013b) to compare their different results as suggested in Pinamonti et al. (2017). The BGLS periodogram results are very similar to those from GLS, with the 9 d peak dominating the first periodogram, and the $P = 23.7$ d signal emerging in the residuals analysis. A difference arises in the second residual analysis compared to the bottom panel of Fig. 3, since the periodic signals are much weaker, with a theoretical BGLS FAP (as defined in Pinamonti et al. 2017) greater than 10%[3]. The FREDEC analysis instead produces as best fit solution the five-signal solution $P_1 = 18.46$ d, $P_2 = 18.10$ d, $P_3 = 9.66$ d ,$P_4 = 9.05$ d, $P_5 = 8.99$ d, with a FAP = 1%. As an alternative but slightly less significant (FAP $\simeq$ 1.5%) solution, the algorithm proposes a four-signal solution $P_1 = 23.71$ d, $P_2 = 17.03$ d, $P_3 = 9.65$ d, $P_4 = 9.04$ d, which includes also the 23.7 d signal found by the other techniques. It is worth noting the presence of multiple periodic signals near the stellar rotation period and its first harmonic, which proves that the RV stellar activity signal is strongly quasi-periodic.

5.2. Stellar activity analysis

To expand the analysis of the stellar activity signals of GJ 685 performed by Suárez Mascareño et al. (2018), we derived the complete time series for all the line profile indicators evaluated with the method from Lanza et al. (2018). These latter authors derived several line profile asymmetry indicators by computing the cross-correlation function (CCF) between a mask and the stellar spectra. For our study, we selected three asymmetry indicators: the bisector inverse span (BIS), ΔV (which compute the difference between the RV values computed with a Gaussian and bi-Gaussian best fit of the CCF, respectively), and $V_{\rm asy}$ (which quantifies the asymmetry in the RV spectral line information content). In addition to this asymmetry analysis, we also derived the activity indexes based on the stellar Ca II H and K, Hα, Na I D_1 D_2, and He I D_3 spectral lines following the procedure described in Gomes da Silva et al. (2011).

As a first-order test of the effect of stellar chromospheric activity on the RV time series, we checked for correlations between the asymmetry and activity indexes, and the RV datasets. We computed the Pearson correlation coefficients for the different combinations of RV and activity indicators, and no significant correlation was identified ($|\rho| \lesssim 0.3$ for all the indexes).

The GLS periodograms of these asymmetry and activity indexes are shown in Figs. 4 and 5. It is worth noting that for the asymmetry indicator $V_{\rm asy}$ we show the results obtained from the new definition by Lanza et al. (2018) ($V_{\rm asy(mod)}$), since, as they stated, the original definition from Figueira et al. (2013) is sensitive to genuine Doppler shifts of the star, and thus presents misleading signals at the periods of actual planets, leading to erroneous rejections.

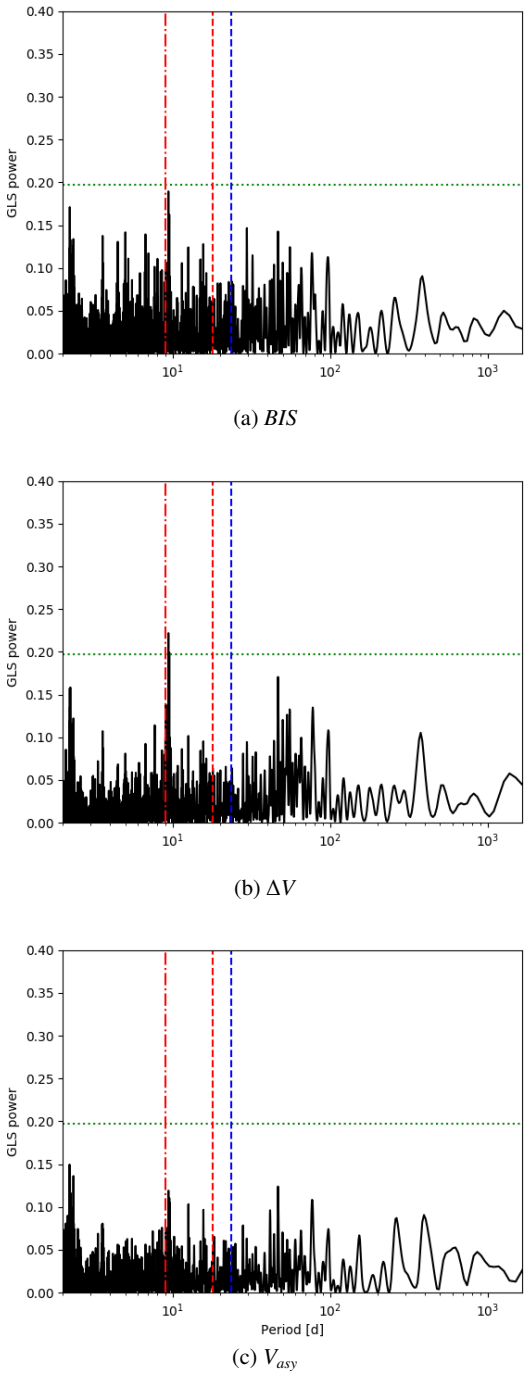

(a) *BIS*

(b) ΔV

(c) V_{asy}

Fig. 4. GLS periodograms of the asymmetry indicators. The red vertical lines indicate the potential rotation period (dashed) and its first harmonic (dot-dashed), while the dashed blue vertical lines mark the orbital period of the planetary candidate discussed in Sect. 5.1. The dotted horizontal lines indicate the 1% FAP level.

We can see in Fig. 4 that the asymmetry indicators show only weak periodic signals, which for two of them, BIS and ΔV, correspond to the first harmonic of the stellar rotation period. In Fig. 5 we see instead that the Ca II H and K and Hα present

[3] For the comparative analysis of the different periodogram algorithms we computed only the theoretical FAPs, since the bootstrap simulation, in particular applied to FREDEC, is very time-consuming.

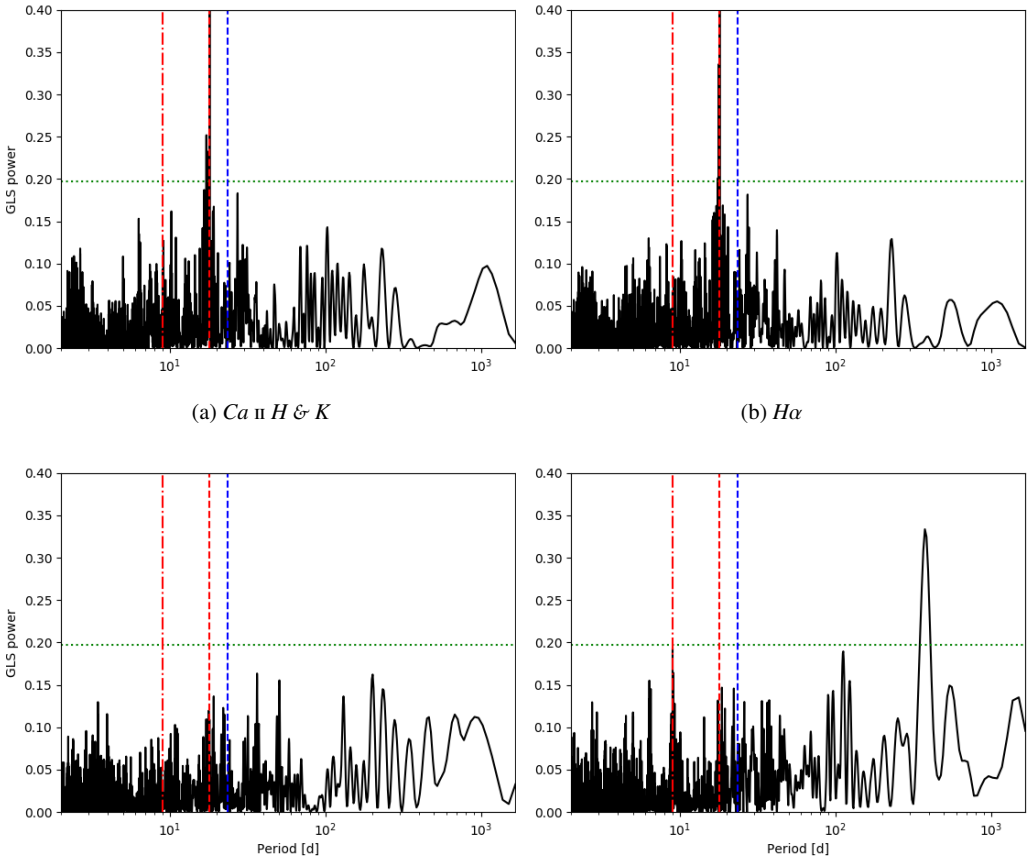

(a) *Ca* II *H & K* (b) *Hα*

(c) *Na* I D_1 D_2 (d) *He* I D_3

Fig. 5. GLS periodograms of the activity indexes. The red vertical lines indicate the potential rotation period (dashed) and its first harmonic (dot-dashed), while the dashed blue vertical lines mark the orbital period of the planetary candidate discussed in Sect. 5.1. The dotted horizontal lines indicate the 1% FAP level.

strong signals corresponding to the stellar rotation, while the He I D_3 index shows only a long-term signal around 400 d[4]. The GLS analysis of the Na I D_1 D_2 time series produces no significant signals.

Our GLS analysis of different asymmetry and activity indicators confirms the results of Suárez Mascareño et al. (2018), providing a slightly longer stellar rotation period of 18 d, with clear signals at both the rotation period and its first harmonic. This confirms the rotation period, $P_{\rm rot} = 18$ d, identified in the RV time series in Sect. 5.1, with respect to the shorter $P_{\rm rot,\,AP} = 16.85$ d found in the APACHE photometric data in Sect. 4.1. Moreover it is worth noting how no peak was identified in the indicators time series at periods corresponding or close to the $P_{\rm b} = 23$ d period of the new planet candidate GJ 685 b.

6. MCMC analysis

We then proceeded to expand our analysis of the RV and activity indexes time series with a combined fit of the Keplerian and stellar activity signals. A very common method to model and subtract the stellar activity correlated "noise" from RV time series is the Gaussian Process (GP) regression (e.g. Haywood et al. 2014; Grunblatt et al. 2015; Dumusque et al. 2017; Pinamonti et al. 2018). This technique has proven to be especially effective when adopting a quasi-periodic covariance function described by four parameters, called hyper-parameters:

$$K(t,t') = h^2 \times \exp\left[-\frac{(t-t')^2}{2\lambda^2} - \frac{\sin^2\left(\frac{\pi(t-t')}{\theta}\right)}{2w^2}\right] + (\sigma^2_{\rm data}(t) + \sigma^2_{\rm jit}) \cdot \delta_{\rm t,t'}, \quad (1)$$

where t and t' indicate two different epochs; h is the amplitude of the correlations; θ represents the period of the correlated signal (and corresponds to the rotation period of the star in our model); w is the length scale of the periodic component; and λ is the correlation decay timescale (which can be related to the decay time of the active regions); $\sigma_{\rm data}(t)$ is the data internal error at time t for each instrument; $\sigma_{\rm jit}$ is the additional uncorrelated "jitter" term used in the analysis of the RVs; and $\delta_{\rm t,t'}$ is the Kronecker delta function.

For a more thorough description of the GP kernel and hyper-parameters, see Pinamonti et al. (2018).

We applied the GP regression as part of an MCMC analysis, performed via the publicly available `emcee` algorithm (Foreman-Mackey et al. 2013) and `GEORGE` Python library (Ambikasaran et al. 2015). We used 150 random walkers to sample the parameter space. The posterior distributions were derived after applying a burn-in as explained in Eastman et al. (2013, and references therein). To evaluate the convergence of the different MCMC analyses, we calculated the integrated correlation time for each of the parameters, and stopped the code after a number of steps equal to 150 times the largest autocorrelation times of all the parameters (Foreman-Mackey et al. 2013).

[4] In the analysis of the residuals of the He I D_3 time series (not shown), only an additional signal at $P = 9$ d emerges, corresponding to the rotation period first harmonic.

Table 2. Priors and best-fit results for the Gaussian process regression analysis of the Hα activity indicator.

Jump parameter	Prior	Best-fit value
h	$\mathcal{U}(0,1.0)$	$0.00146^{+0.00013}_{-0.00011}$
λ (days)	$\log \mathcal{U}(1,3\,000)$	53^{+16}_{-47}
w	$\mathcal{U}(0,1)$	$0.080^{+0.025}_{-0.011}$
θ (days)	$\mathcal{U}(5,30)$	$17.34^{+0.13}_{-0.05}$
Offset	$\mathcal{U}(-1.0,3.0)$	$0.06188^{+0.00018}_{-0.00018}$

6.1. Activity indexes GP analysis

First we performed a GP emcee fit of the activity index time series, as a reference for the following GP+planetary signal analysis of the RV time series. We show only the Hα time series because, as shown in Fig. 5, the stellar rotation signal of the star is clearly present in the time series, and some studies also suggest the Hα to be the best indicators of the activity of early- and mid-M type stars (e.g. Robertson et al. 2013). We nonetheless also performed an emcee analysis of the Ca II H and K time series (not shown), which produced analogous results.

We chose uniform priors for all the GP hyper-parameters. For the λ hyper-parameter, which represents the correlation decay timescale, and can range over several orders of magnitude, we adopted a uniform prior in logarithmic scale to avoid oversampling the long scales. The adopted priors and best-fit results for the GP hyper-parameters of the analysis are listed in Table 2, while the a posteriori distributions are shown in Fig. 6.

The GP fit confirms that the rotation period of the star, corresponding to the hyper-parameter θ, is close to ∼18 d, as inferred from the GLS analysis. It is also worth noting that the median value of the λ hyper-parameter, which is related to the evolution timescale of the active regions, is of the order of three to four times the rotation period. This is consistent with an independent analysis of a few M dwarfs in the HADES sample reported in Scandariato et al. (2017). The uncertainties of this hyper-parameter are very large due to the tail of the distribution at short timescales, which can be observed in Fig. 6. However, this uncertainty does not affect the determination of the rotation period θ, which is well constrained within a 1 d interval. In addition, this analysis does not present any evidence of longer-period signals in the activity indexes of GJ 685, in particular around the candidate planet period $P_b = 24$ d.

6.2. emcee analysis of the RV time series

To better understand the structure of the stellar activity signal in the RV time series we performed a GP analysis of the dataset, adopting very similar priors to those adopted in the analysis of the Hα activity index time series (see Table 2), and also adding an uncorrelated jitter term to the model. In Table 3 we can see the chosen priors and the best fit values. Since from the analysis of the Hα time series no evidence emerged of long correlation decay timescales, we restricted the prior of λ in the interval $[1, 500]$ d, again uniform in logarithmic space. Even though the analysis of the activity and asymmetry indexes in the previous sections pointed out the absence of stellar activity signals at periods larger than 20 d and in particular close to the orbital period of the planet candidate, we decided to keep the prior of the rotation period θ over the interval $[5, 30]$ d, as in the analysis described in the previous section. In this analysis, we add an uncorrelated jitter term $\sigma_{\rm jit}$, which takes into account any additional uncorrelated stellar noise that is not corrected by the GP model. This can also be used to take into account possible residual errors from the instrumental drift correction (see Sect. 2) as done in Affer et al. (2019).

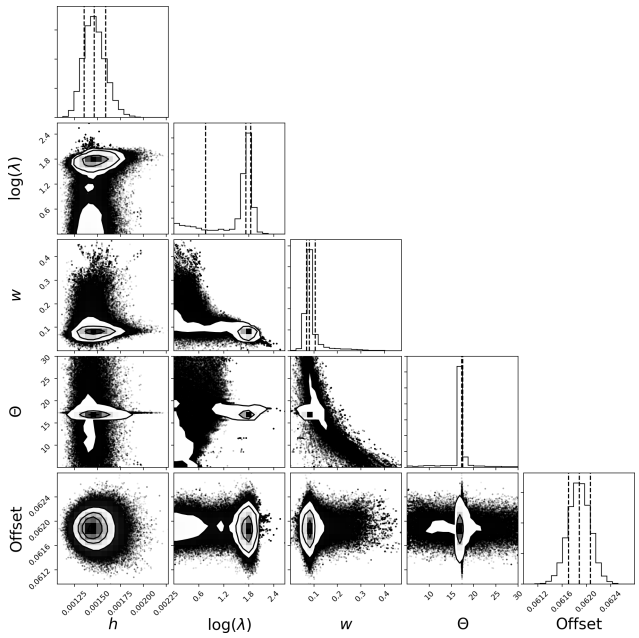

Fig. 6. Posterior distributions of the fitted (hyper-)parameters of the GP quasi-periodic model applied to the time series of Hα activity index. The vertical dashed lines denote the median and the 16th and 84th percentiles.

Table 3. Priors and best-fit results for the emcee analysis of GJ 685 RV time series.

Jump parameter	Prior	Best-fit value	
		Pure GP	GP + planet
h (m s^{-1})	$\mathcal{U}(0,10)$	$6.20^{+0.80}_{-0.66}$	$6.05^{+0.94}_{-0.72}$
λ (days)	$\log \mathcal{U}(1,500)$	$25.4^{+6.0}_{-4.5}$	59^{+18}_{-14}
w	$\mathcal{U}(0,1)$	$0.312^{+0.046}_{-0.040}$	$0.315^{+0.045}_{-0.041}$
θ (days)	$\mathcal{U}(5,30)$	$18.30^{+0.37}_{-0.32}$	$18.15^{+0.15}_{-0.16}$
Offset (m s^{-1})	$\mathcal{U}(-5.0,5.0)$	$0.7^{+1.1}_{-1.1}$	$0.3^{+1.2}_{-1.3}$
Jitter (m s^{-1})	$\mathcal{U}(0.0,10.0)$	$1.41^{+0.43}_{-0.38}$	$1.46^{+0.33}_{-0.32}$
Acceleration (m s^{-1} d)	$\mathcal{U}(-0.05,0.05)$	$0.0002^{+0.0020}_{-0.0020}$	$0.0010^{+0.0024}_{-0.0024}$
k (m s^{-1})	$\mathcal{U}(0,5.0)$	–	$3.00^{+0.53}_{-0.52}$
P (days)	$\mathcal{U}(20.0,100.0)$	–	$24.160^{+0.061}_{-0.047}$
T_0 (phase)	$\mathcal{U}(0.0,1.0)$	–	$0.24^{+0.11}_{-0.10}$
Derived parameter			
$M_P \sin i$ ($M_\oplus$)	–	–	$9.0^{+1.7}_{-1.8}$
a_P (AU)	–	–	$0.1344^{+0.0052}_{-0.0051}$

In Fig. 7 the posterior distributions of the fit parameters are shown. We can see that, even if the GLS periodogram identifies $P = 9$ d as the strongest period, the GP correctly identifies the 18 d rotation period of the star, taking into account the complex nature of the stellar activity RV signal due to its quasi-periodic nature. It is also worth noting from Table 3 that the value found in this analysis for the hyper-parameter λ is smaller than the one

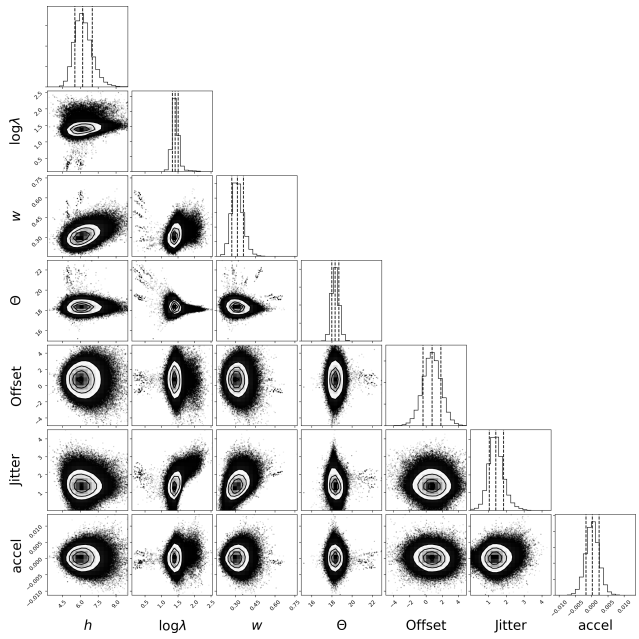

Fig. 7. Posterior distributions of the fitted (hyper-)parameters of the pure GP model applied to the RV time series. The vertical dashed lines denote the median and the 16 th and 84 th percentiles.

previously found in the analysis of the Hα index time series, even though it remains consistent within the large error bars.

We then repeated the emcee analysis adding a Keplerian planetary signal to the model, to recover the best-fit parameters of the candidate planet GJ 685 b. We used wide priors for the planetary parameters, so as not to force the solution on the value found with the GLS periodogram, with the prior of the orbital period ranging up to 100 d. For the same reason, the priors on the planetary parameters were all chosen to be uninformative uniform priors. We can see the best-fit solution in the right column of Table 3, while the posterior distributions are shown in Fig. 8. It is worth noting that, while the amplitude of the signal is quite similar to the value recovered from the periodogram analysis, the period is slightly longer, due to the simultaneous fitting of the stellar activity signal with the GP. A series of aliases of the orbital period P appear to be present, slightly correlated with T_0, in the bottom right contour plot in Fig. 8. However, as we can see in the histograms of the posterior distributions of the orbital parameters, these aliases are not significant and do not change the best-fit value of the orbital period. Moreover, we can see in the right column of Table 3 that the best-fit value of λ is larger than in the pure GP analysis (left column), and much more similar to that found in the analysis of the Hα: this can be explained by the fact that in the pure-GP model the presence of the un-modelled planetary signal interferes with the fit of the stellar activity, and a shorter decay timescale is needed to compensate this effect. Once the planetary signal is taken into account in the analysis, the decay timescale returns to the more accurate value found in the activity index analysis. It is also worth noting that the jitter term retrieved by the emcee analysis is small, $\sigma_{\rm jit} = 1.46^{+0.33}_{-0.32}$ m s^{-1}, suggesting low levels of uncorrelated stellar noise, as well as confirming the low levels of residual instrumental drift as discussed in Sect. 2.

The quasi-periodic stellar model obtained from the simultaneous GP + 1 planet fit is shown in Fig. 9 compared to the RV time series residuals after the subtraction of the 24 d planetary signal. We can see both the fine correspondence between the data and our stellar model, and the strength and variability of the stellar signals throughout the four years of HADES observations.

As additional evidence of the presence of the candidate planet GJ 685 b, we computed the Bayesian information criterion (BIC, Schwarz et al. 1978) for the two models, obtaining BIC = 635 and BIC = 619 for the pure GP and GP + 1 planet models, respectively. There is a very strong statistical evidence, ΔBIC = 16, in favour of the presence of the planetary signal. Figure 10 shows the phase-folded RV time series, closely following the planetary model after subtraction of the stellar activity signal.

In Table 3 are also shown the values of minimum mass, $M_{\rm P} \sin i$, and semi-major axis, $a_{\rm P}$, derived from the best-fit orbital parameters of the GP + planet model. The derived minimum mass is $9.0^{+1.7}_{-1.8}$ $M_\oplus$, placing GJ 685 b within the Super-Earth regime. Since single-planet systems are known to show a wide range of eccentricities (e.g. Rodigas & Hinz 2009; Limbach & Turner 2015), we also tested an eccentric model for GJ 685 b in order to constrain the possible eccentricity of the orbit. This additional analysis resulted in a best-fit value of $e = 0.14^{+0.18}_{-0.10}$, consistent with zero within 1.5-σ, and also with a higher value of BIC = 628 with respect to the circular model.

We found no evidence for the presence of additional short-period signals in the RV time series: we computed the GLS periodogram of the RV residuals after the subtraction of the GP + 1 planet model, and no significant signal below the 10% FAP level was found. Additionally, we tested a GP + 2 planets MCMC model, with the parameters of the second planet left free to explore a wide parameter space; we did not find any dominant signal and no statistical improvement of its BIC over the GP + 1 planet model. Moreover, as reported in Table 3, the best-fit value of the acceleration in our final model is 0.0010 ± 0.0024 m s^{-1} d^{-1}, largely consistent with zero, suggesting the absence of long-period signals.

7. Summary and discussion

We investigated 106 spectroscopic observations of GJ 685 obtained over 4.4 yr with HARPS-N at the TNG in La Palma and additional photometry from the APACHE and EXORAP programs. We used RVs derived from the TERRA pipeline along with activity and asymmetry indexes derived from the same HARPS-N spectra and used them to monitor the stellar chromospheric activity of the target.

The RV time series of GJ 685 is dominated by three peaks at 9, 18, and 24 d. Our spectroscopic analysis, strengthened by the analyses of two independent photometric light curves of the target, confirms that the 18 and 9d period signals are related to the stellar activity, corresponding respectively to the stellar rotation period and its first harmonic. On the other hand, the 24 d period signal seems not to be related to any stellar effects, and is best described as a Keplerian signal caused by an orbiting planet, GJ 685 b.

To derive the minimum mass and orbital parameters of GJ 685 b we fitted the RV time series with a Keplerian model combined with a GP quasi-periodic model to take into account the stellar activity signal. We obtained a period $P_{\rm b} = 24.160$ d, a semi-major axis $a = 0.1344$ AU, and a minimum mass $M_{\rm b} \sin i = 9.0$ $M_\oplus$. The GP quasi-periodic model improves the precision of the rotation period of the stars computed by Suárez Mascareño et al. (2018), finding a best-fit value of $18.15^{+0.15}_{-0.16}$ d. The amplitude of the stellar activity signal is $h = 6.05^{+0.94}_{-0.72}$ m s^{-1}, more than twice the amplitude of the Keplerian signal of GJ 685 b, similar to the case of GJ 3942 (Perger et al. 2017a).

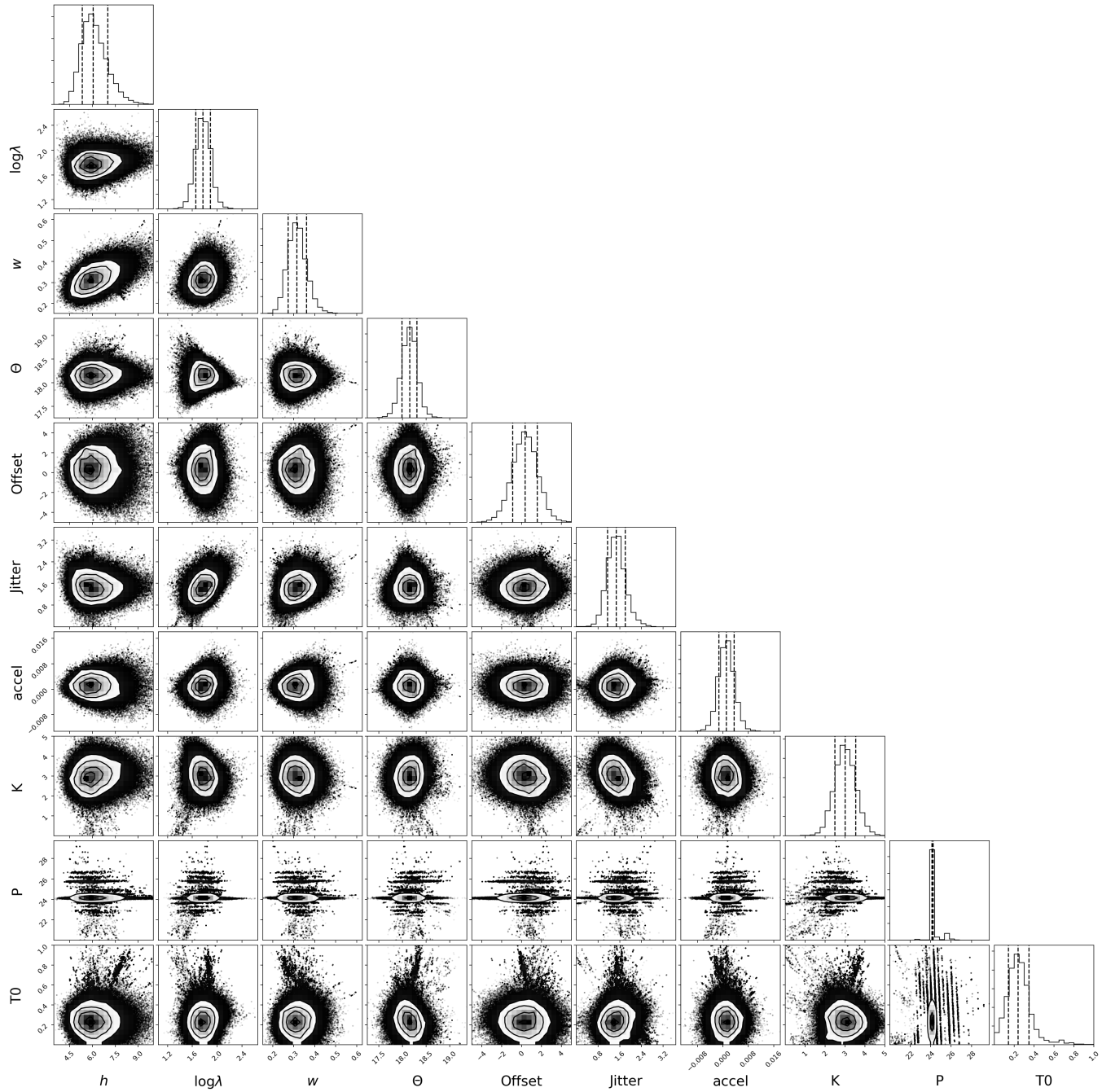

Fig. 8. Posterior distributions of the fitted (hyper-)parameters of the GP + 1 planet model applied to the RV time series. The vertical dashed lines denote the median and the 16th and 84th percentiles.

It is also worth noting that GJ 685 presents the largest stellar RV signal of the HADES targets with planetary companions detected to date. Moreover, even if the strongest periodic signal present in the RV time series is the rotation period first harmonic, $P_{\rm rot/2} = 9$ d, the GP model easily identifies the actual rotation period of the star, $P_{\rm rot} = 18$ d, as the source of the RV modulation. Even though the prior adopted for the θ hyperparameter was very wide, including also the first harmonic value of 9 d, the model converged naturally on the rotation period. This again demonstrates the effectiveness of GP quasi-periodic models when dealing with complex stellar activity signals producing several different peaks in the periodogram, even if the strongest peak does not correspond to the stellar rotation period.

We tested an eccentric model for the orbit of GJ 685 b. A single-planet system could be expected to show significant eccentricity, since the orbit of this planet should not be circularized by tides owing to the relatively large separation from the star. The analysis resulted in a best-fit value of eccentricity consistent with zero within 1.5-σ, and a posterior distribution (not shown) strongly peaked at zero. Moreover, the BIC presented strong statistical evidence in favour of the circular-orbit model. We therefore adopted the null-eccentricity model as the best representation of the orbit of GJ 685 b.

Due to its close orbit to the host star, GJ 685 b is unlikely to host an atmosphere capable of maintaining liquid water on its surface. Following the definition of habitable zone (HZ) from

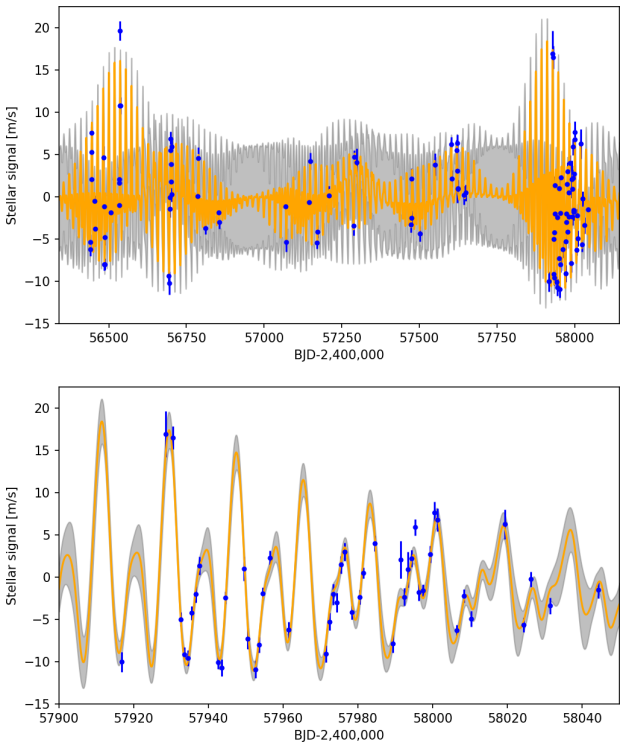

Fig. 9. *Upper panel*: best-fit stellar quasi-periodic signal obtained from the GP + 1 planet model (orange line) compared to the RV residuals (blue points). *Lower panel*: magnification of the last HARPS-N observing season. The grey area represents the $\pm 1\sigma$ uncertainties of the stellar activity model.

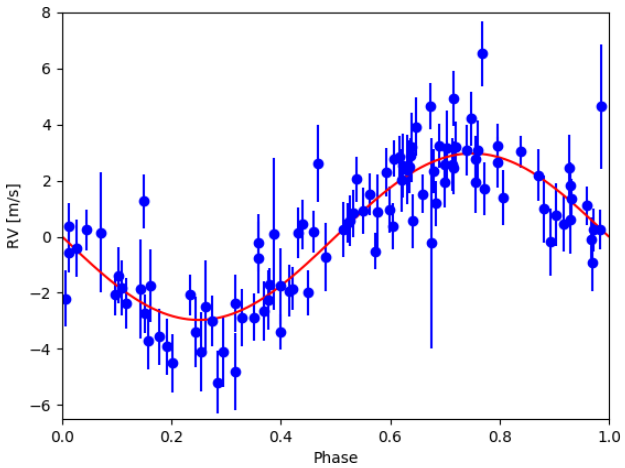

Fig. 10. Phase-folded for the RV signal of GJ 685 b, after the subtraction of the stellar correlated signal.

Kopparapu et al. (2013), we computed the inner edge of the HZ for GJ 685, with the most optimistic limits ("recent Venus"), which correspond to a semi-major axis of $a_{\rm HZ} = 0.190$ AU, significantly larger than the orbit of GJ 685 b.

GJ 685 b is the seventh extrasolar planet discovered within the HADES program (Affer et al. 2016, 2019; Suárez Mascareño et al. 2017; Perger et al. 2017a; Pinamonti et al. 2018). Figures 11 and 12 show GJ 685 b and the other HADES planets compared to the current population of RV detected planets orbiting M dwarfs selected from the NASA Exoplanet Archive[5]: the sample is composed of 70 extrasolar planets discovered with the RV method and orbiting stars of spectral type M0 and M9. Even if the sample is relatively small, some information can be gleaned concerning the planetary and stellar parameters of these systems. First of all, it is worth noting that there seems to be no high-mass planets orbiting low-mass late-type M dwarfs (bottom-left panel Fig. 11). Similarly, there seems to be a scarcity of long-period planets orbiting stars with $M_* < 0.3\ M_\odot$, which is the same threshold below which only low-mass planets have been detected. However, these effects are strongly affected by observational bias, since late-type M dwarfs are very faint and difficult to observe, and therefore are usually excluded from RV exoplanet surveys; for example the HADES sample has a median stellar mass of $0.5\,M_\odot$, with no target below $0.3\,M_\odot$ (Perger et al. 2017b). This bias should be solved in the near future, since RV surveys such as CARMENES (Quirrenbach et al. 2014) and SPIRou (Moutou et al. 2017) are intensively monitoring large samples of nearby M dwarfs in search of extrasolar planets; the CARMENES sample for example includes ≃120 stars with $M_* < 0.3\ M_\odot$ (Reiners et al. 2018). Nevertheless, to date no such high-mass planet has been announced.

It is also worth noting from the bottom-right panel of Fig. 11 that there appears to be a dependence of the planetary minimum mass on the stellar metallicity: we computed the Pearson correlation coefficient, which found a weak-to-moderate correlation, $\rho = 0.30$ p-value = 1.5%. A similar dependence is expected from theoretical models (e.g. Mordasini et al. 2012) and was observed also for solar-mass dwarf stars (e.g. Mortier et al. 2012; Wang & Fischer 2015), while not for planet-hosting giants (Mortier et al. 2013). Moreover, although this effect was observed to be strong for giant planets, which are much more abundant around high-metallicity stars (e.g. Santos et al. 2005; Gaidos & Mann 2014), it is still debated for low-mass Neptune-like planets and super-Earths: some studies found no evidence of a correlation between metallicity and planetary occurrence rates for such small planets (e.g. Sousa et al. 2008; Gaidos et al. 2016), while Wang & Fischer (2015), analysing a large sample of *Kepler*-candidates, pointed out that a similar correlation should be present, though weakened, down to terrestrial planets. Courcol et al. (2016) studied a sample of mass-measured exoplanets, and found evidence for the frequency of exo-Neptunes ($M \in [10, 40]\ M_\oplus$) to be correlated with stellar metallicity, while this was not the case for super-Earths ($M < 10\ M_\oplus$). Similarly, we could divide our sample of RV-detected planets between masses higher and lower than $10\ M_\oplus$ (green dashed line in the bottom-right panel of Fig. 11): the two sub-samples have both weaker correlations, $\rho = 0.23$ p-value = 30% for $M > 10\ M_\oplus$, and $\rho = 0.22$ p-value = 14% for $M < 10\ M_\oplus$. However, the high-mass subsample contains only 22 planets, which could be the cause of the non-detection of the expected correlation. Therefore, based on the selected sample, we are not able to confirm whether or not the trend observed by Courcol et al. (2016) affects M dwarfs in the same way as solar-mass stars.

Analysing only the subsample of exoplanets discovered by the HADES program it is difficult to confirm the properties discussed above. The HADES planets are mostly found in a small region of the parameter space, since they usually have low masses and relatively short periods. Also, by construction of the survey, HADES targets are in narrow ranges of stellar parameters (Perger et al. 2017b; Maldonado et al. 2017). This will allow a focused analysis of the characteristics of planetary systems around specific stellar hosts, and more results will become available as the analysis of the complete survey sample draws near. It is worth noting that the distribution of HADES planets is not surprising, since they are mostly found near the medians

[5] https://exoplanetarchive.ipac.caltech.edu/ – 18/12/2018.

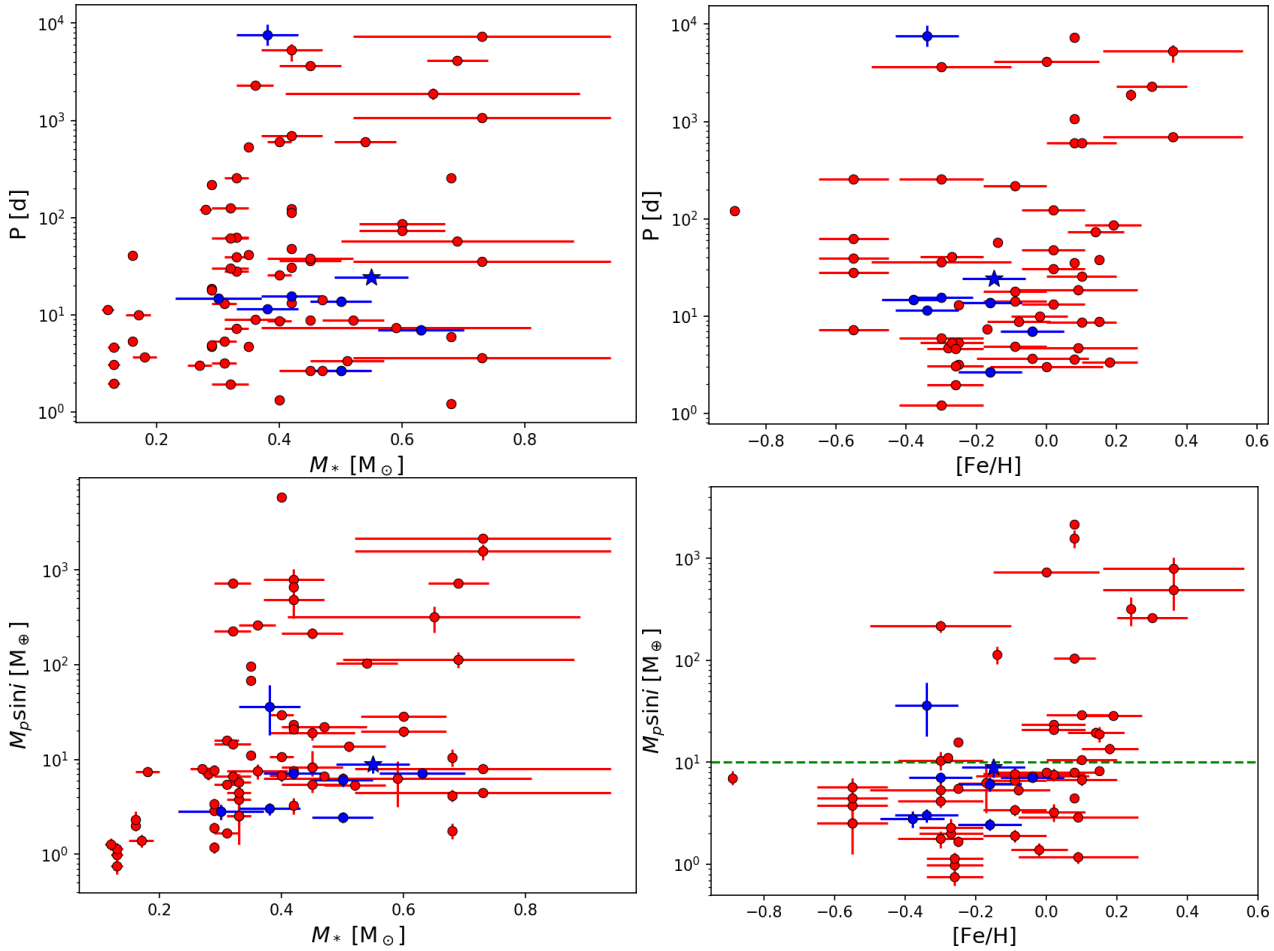

Fig. 11. Properties of RV exoplanets orbiting M dwarfs. *Top-left panel*: orbital period as a function of the mass of the host star. *Top-right panel*: orbital period as a function of the metallicity of the host star. *Bottom-left panel*: minimum mass as a function of the mass of the host star. *Bottom right panel*: minimum mass as a function of the metallicity of the host star. The red dots represent the M-dwarf hosted RV extrasolar planets, the blue dots represent the HADES planets, and the blue star represents the newly detected planet GJ 685 b.

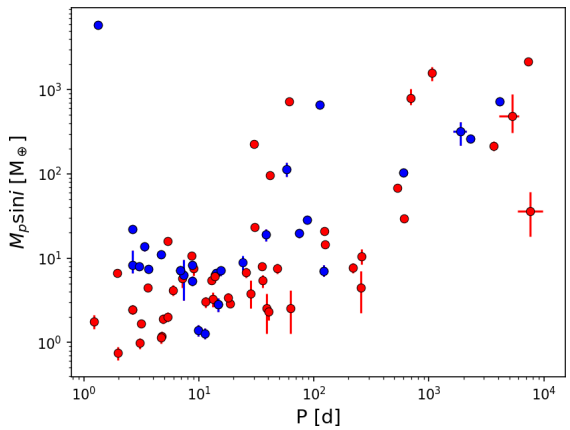

Fig. 12. Properties of RV exoplanets orbiting M dwarfs. Minimum mass as a function of the orbital period of the planet. The red dots represent planets orbiting M dwarfs in multiple systems, while the blue dots represent single planets.

of the overall period and minimum mass distributions, $\tilde{P} = 19$ d $\tilde{M} \sin i = 7.6\ M_\oplus$.

Recently, Luque et al. (2018) suggested that masses of single and multiple systems around M dwarfs should follow different distributions. To test this hypothesis, Fig. 12 shows the minimum masses and orbital periods of our sample of M-dwarfs planets, distinguishing between single and multiple planetary systems. We can observe that the two populations appear to have similar distributions, with the single planets being on average slightly more massive than those found in multiple systems[6]. To asses the statistical significance of this difference, we performed a two-sided Kolmogorov-Smirnov (K-S) test of the minimum mass distributions of the two populations. We obtained a p-value $p = 1.3\%$, thus reinforcing our hypothesis that planets found in multi- and single-planet systems tend to have different masses. This seems to confirm the effect found by Luque et al. (2018), who studied a different sample of M-dwarf extrasolar planets with masses measured from RVs and TTVs. These latter authors suggested two possible explanations, connected to the formation of low-mass planets: that either (i) the formation of super-Earth impedes the formation of smaller Earth-like planets in the same system, or (ii) super-Earth planets around M dwarfs are formed by a pile-up of several low-mass planets. If the former were true, the single more-massive planet populations would have a mass distribution lower than that of the summed mass of the planets in multiple systems, due to the absence of additional smaller-mass planets not able to form. We tested this hypothesis on our

[6] The minimum mass distribution of detected exoplanets could be affected by observation bias, hiding the presence of additional undetected companions.

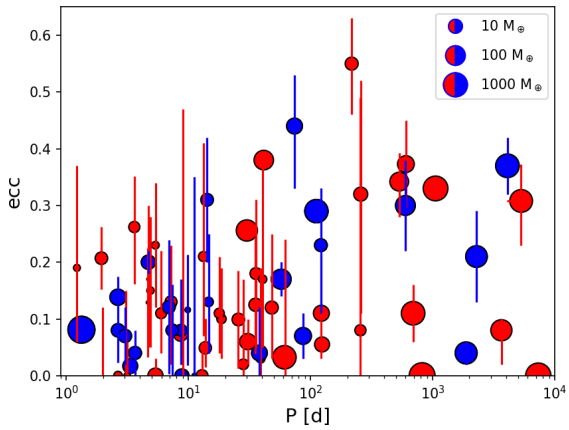

Fig. 13. Properties of RV exoplanets orbiting M dwarfs. Orbital eccentricity as a function of the orbital period of the planet. The red dots represent planets orbiting M dwarfs in multiple systems, while the blue dots represent single planets. The marker size represents the minimum mass of the planet.

dataset, performing another K-S test on the two distributions, and obtained a very high p-value $p = 47\%$. We found no evidence in favour of the first formation mechanism proposed by Luque et al. (2018), suggesting that M-dwarf super-Earths are formed by aggregation of smaller planets.

To further compare the properties of the single- and multi-planet populations around M dwarfs, Fig. 13 shows the eccentricities and orbital periods of the planets in the considered sample. Several studies pointed out a wide distribution of orbital eccentricities of exoplanets, as well as significant correlation with orbital periods (e.g. Stepinski & Black 2000; Kipping 2013) and multiplicities (e.g. Rodigas & Hinz 2009; Limbach & Turner 2015). We can see in Fig. 13 that, even if the observed distribution of exoplanets orbiting solar-type stars extend up to $e \sim 0.9$, for M-dwarf RV planets the eccentricities are usually $e < 0.5$, even for long-period giant planets. Moreover, comparing the single- and multi-planet populations, we find no difference in their eccentricity distribution; they are very similar, with a K-S test suggesting the two distributions to be identical (p-value $p = 99\%$). This is further evidence of the difference between the populations of extrasolar planets orbiting M dwarfs and solar-type stars. Focusing on the sub-sample of low-mass planets ($M_p \sin i < 30\ M_\oplus$), it is worth noting that eccentricities are usually poorly constrained: out of 54 low-mass planets, only 7 have eccentricities with a significance higher than 3-σ. This is not surprising, since eccentricities are often difficult to precisely constrain, in particular for single-planet systems (e.g. Wittenmyer et al. 2013).

In Fig. 12, there also appears to be a correlation between the minimum mass and the orbital period, as was suggested by early formation models (Zucker & Mazeh 2002, and references therein). However, the Pearson correlation coefficient does not favour such a correlation in our sample: $\rho = 0.22$ p-value = 5.0%. It is also important to note that observational biases have a strong influence on the mass and period distributions, since smaller-mass and longer-period planets are more difficult to detect. Recent studies on the occurrence rates of extrasolar planets around M dwarfs, taking into account detection probabilities and detection biases, suggest that low-mass long-period planets could in fact be abundant around M dwarfs (Bonfils et al. 2013; Tuomi et al. 2014), but such an extended analysis is beyond the scope of this paper. Moreover, it is worth noting that M stars are a very heterogeneous group, with early- and late-M dwarfs differing in both their internal structure and magnetic activity. Therefore, a more accurate study of the properties of planetary systems around low-mass stars should consider different early- and late-M stars separately. For this reason, the target of the HADES programme is precisely to study the population of extrasolar planets over a well-defined sample of targets with similar spectral type and stellar properties.

A thorough and unbiased analysis of the detection efficiencies and planetary occurrence rates in the HADES sample, completing and expanding the preliminary statistical analysis from Perger et al. (2017b), will be the object of a future publication (Pinamonti et al., in prep.).

Acknowledgements. GAPS acknowledges support from INAF through the Progetti Premiali funding scheme of the Italian Ministry of Education, University, and Research. M.Pi. gratefully acknowledges the support from the European Union Seventh Framework Programme (FP7/2007-2013) under Grant Agreement No. 313014 (ETAEARTH). L.A., A.F.L., G.M., J.M., and M.D. acknowledge financial support from Progetto Premiale 2015 FRONTIERA funding scheme of the Italian Ministry of Education, University, and Research. G.S. acknowledges financial support from "Accordo ASI-INAF" No. 2013-016-R.0 July 9, 2013 and July 9, 2015. M.Pe. and I.R. acknowledge support from the Spanish Ministry of Economy and Competitiveness (MINECO) and the Fondo Europeo de Desarrollo Regional (FEDER) through grant ESP2016-80435-C2-1-R, as well as the support of the Generalitat de Catalunya/CERCA program. J.I.G.H., R.R. and B.T.P. acknowledge financial support from the Spanish Ministry project MINECO AYA2017-86389-P, and J.I.G.H. from the Spanish MINECO under the 2013 Ramón y Cajal programme MINECO RYC-2013-14875. This work is based on observations made with the Italian Telescopio Nazionale *Galileo* (TNG), operated on the island of La Palma by the Fundación Galielo Galilei of the Istituto Nazionale di Astrofisica (INAF) at the Spanish Observatorio del Roque de los Muchachos (ORM) of the Instituto de Astrofísica de Canarias (IAC). This work has made use of data from the European Space Agency (ESA) mission *Gaia* (`https://www.cosmos.esa.int/gaia`), processed by the *Gaia* Data Processing and Analysis Consortium (DPAC, `https://www.cosmos.esa.int/web/gaia/dpac/consortium`). Funding for the DPAC has been provided by national institutions, in particular the institutions participating in the *Gaia* Multilateral Agreement.

References

Affer, L., Micela, G., Damasso, M., et al. 2016, A&A, 593, A117
Affer, L., Damasso, M., Micela, G., et al. 2019, A&A, 622, A193
Ambikasaran, S., Foreman-Mackey, D., Greengard, L., Hogg, D. W., & O'Neil, M. 2015, IEEE Trans. Pattern Anal. Mach. Intell., 38, 2
Anglada-Escudé, G., & Butler, R. P. 2012, ApJS, 200, 15
Anglada-Escudé, G., Amado, P. J., Barnes, J., et al. 2016a, Nature, 536, 437
Anglada-Escudé, G., Tuomi, M., Arriagada, P., et al. 2016b, ApJ, 830, 74
Astudillo-Defru, N., Forveille, T., Bonfils, X., et al. 2017a, A&A, 602, A88
Astudillo-Defru, N., Díaz, R. F., Bonfils, X., et al. 2017b, A&A, 605, L11
Astudillo-Defru, N., Delfosse, X., Bonfils, X., et al. 2017c, A&A, 600, A13
Baluev, R. V. 2013a, MNRAS, 429, 2052
Baluev, R. V. 2013b, Astron. Comput., 3, 50
Bonfils, X., Mayor, M., Delfosse, X., et al. 2007, A&A, 474, 293
Bonfils, X., Delfosse, X., Udry, S., et al. 2013, A&A, 549, A109
Cosentino, R., Lovis, C., Pepe, F., et al. 2012, in Ground-based and Airborne Instrumentation for Astronomy IV, Proc. SPIE, 8446, 84461V
Courcol, B., Bouchy, F., & Deleuil, M. 2016, MNRAS, 461, 1841
Covino, E., Esposito, M., Barbieri, M., et al. 2013, A&A, 554, A28
Cutri, R. M., Skrutskie, M. F., van Dyk, S., et al. 2003, VizieR Online Data Catalog: II/246
Desidera, S., Sozzetti, A., Bonomo, A. S., et al. 2013, A&A, 554, A29
Dressing, C. D., & Charbonneau, D. 2013, ApJ, 767, 95
Dumusque, X., Lovis, C., Udry, S., & Santos, N. C. 2011, in The Astrophysics of Planetary Systems: Formation, Structure, and Dynamical Evolution, eds. A. Sozzetti, M. G. Lattanzi, & A. P. Boss, IAU Symp., 276, 530
Dumusque, X., Boisse, I., & Santos, N. C. 2014, ApJ, 796, 132
Dumusque, X., Borsa, F., Damasso, M., et al. 2017, A&A, 598, A133
Eastman, J., Gaudi, B. S., & Agol, E. 2013, PASP, 125, 83
Endl, M., Kürster, M., Els, S., Hatzes, A. P., & Cochran, W. D. 2001, A&A, 374, 675
Figueira, P., Santos, N. C., Pepe, F., Lovis, C., & Nardetto, N. 2013, A&A, 557, A93

Foreman-Mackey, D., Hogg, D. W., Lang, D., & Goodman, J. 2013, PASP, 125, 306
Forveille, T., Bonfils, X., Delfosse, X., et al. 2009, A&A, 493, 645
Gaia Collaboration (Brown, A. G. A., et al.) 2018, A&A, 616, A1
Gaidos, E., & Mann, A. W. 2014, ApJ, 791, 54
Gaidos, E., Mann, A. W., Kraus, A. L., & Ireland, M. 2016, MNRAS, 457, 2877
Giacobbe, P., Damasso, M., Sozzetti, A., et al. 2012, MNRAS, 424, 3101
Giampapa, M. S., Cram, L. E., & Wild, W. J. 1989, ApJ, 345, 536
Gomes da Silva, J., Santos, N. C., Bonfils, X., et al. 2011, A&A, 534, A30
González-Álvarez, E., Micela, G., Maldonado, J., et al. 2019, A&A, 624, A27
Grunblatt, S. K., Howard, A. W., & Haywood, R. D. 2015, ApJ, 808, 127
Haywood, R. D., Collier Cameron, A., Queloz, D., et al. 2014, MNRAS, 443, 2517
Kipping, D. M. 2013, MNRAS, 434, L51
Kopparapu, R. K., Ramirez, R., Kasting, J. F., et al. 2013, ApJ, 765, 131
Kürster, M., Endl, M., Rouesnel, F., et al. 2003, A&A, 403, 1077
Lanza, A. F., Malavolta, L., Benatti, S., et al. 2018, A&A, 616, A155
Laughlin, G., Bodenheimer, P., & Adams, F. C. 2004, ApJ, 612, L73
Limbach, M. A., & Turner, E. L. 2015, Proc. Natl. Acad. Sci., 112, 20
Lovis, C., & Pepe, F. 2007, A&A, 468, 1115
Luque, R., Nowak, G., Pallé, E., et al. 2018, A&A, 620, A171
Maldonado, J., Affer, L., Micela, G., et al. 2015, A&A, 577, A132
Maldonado, J., Scandariato, G., Stelzer, B., et al. 2017, A&A, 598, A27
Mayor, M., Pepe, F., Queloz, D., et al. 2003, The Messenger, 114, 20
Mordasini, C., Alibert, Y., & Benz, W. 2009, A&A, 501, 1139
Mordasini, C., Alibert, Y., Benz, W., Klahr, H., & Henning, T. 2012, A&A, 541, A97
Mortier, A., Santos, N. C., Sozzetti, A., et al. 2012, A&A, 543, A45
Mortier, A., Santos, N. C., Sousa, S. G., et al. 2013, A&A, 557, A70
Mortier, A., Faria, J. P., Correia, C. M., Santerne, A., & Santos, N. C. 2015, A&A, 573, A101
Moutou, C., Vigan, A., Mesa, D., et al. 2017, A&A, 602, A87
Perger, M., Ribas, I., Damasso, M., et al. 2017a, A&A, 608, A63
Perger, M., García-Piquer, A., Ribas, I., et al. 2017b, A&A, 598, A26
Perger, M., Scandariato, G., Ribas, I., et al. 2019, A&A, 624, A123
Pinamonti, M., Sozzetti, A., Bonomo, A. S., & Damasso, M. 2017, MNRAS, 468, 3775
Pinamonti, M., Damasso, M., Marzari, F., et al. 2018, A&A, 617, A104
Poretti, E., Boccato, C., Claudi, R., et al. 2016, Mem. Soc. Astron. It., 87, 141
Queloz, D., Henry, G. W., Sivan, J. P., et al. 2001, A&A, 379, 279
Quirrenbach, A., Amado, P. J., Caballero, J. A., et al. 2014, in Ground-based and Airborne Instrumentation for Astronomy V, Proc. SPIE, 9147, 91471F
Reiners, A., Zechmeister, M., Caballero, J. A., et al. 2018, A&A, 612, A49
Robertson, P., Endl, M., Cochran, W. D., & Dodson-Robinson, S. E. 2013, ApJ, 764, 3
Robertson, P., Mahadevan, S., Endl, M., & Roy, A. 2014, Science, 345, 440
Robertson, P., Roy, A., & Mahadevan, S. 2015, ApJ, 805, L22
Rodigas, T. J., & Hinz, P. M. 2009, ApJ, 702, 716
Santos, N. C., Israelian, G., Mayor, M., et al. 2005, A&A, 437, 1127
Scandariato, G., Maldonado, J., Affer, L., et al. 2017, A&A, 598, A28
Schwarz, G. 1978, Ann. Stat., 6, 461
Sousa, S. G., Santos, N. C., Mayor, M., et al. 2008, A&A, 487, 373
Sozzetti, A., Bernagozzi, A., Bertolini, E., et al. 2013, Eur. Phys. J. Web Conf., 47, 03006
Stepinski, T. F., & Black, D. C. 2000, A&A, 356, 903
Suárez Mascareño, A., González Hernández, J. I., Rebolo, R., et al. 2017, A&A, 605, A92
Suárez Mascareño, A., Rebolo, R., González Hernández, J. I., et al. 2018, A&A, 612, A89
Tamuz, O., Ségransan, D., Udry, S., et al. 2008, A&A, 480, L33
Tuomi, M., Jones, H. R. A., Barnes, J. R., Anglada-Escudé, G., & Jenkins, J. S. 2014, MNRAS, 441, 1545
Valenti, J. A., & Fischer, D. A. 2005, VizieR Online Data Catalog: J/ApJS/159/141
Wang, J., & Fischer, D. A. 2015, AJ, 149, 14
Wittenmyer, R. A., Wang, S., Horner, J., et al. 2013, ApJS, 208, 2
Zechmeister, M., & Kürster, M. 2009, A&A, 496, 577
Zucker, S., & Mazeh, T. 2002, ApJ, 568, L113

Appendix A: Observation log for GJ 685

In this section we report the observational data collected with the HARPS-N spectrograph as part the HADES project and used in the present study. We list in Table A.1 the observation dates (barycentric Julian date or BJD), the RVs calculated by the TERRA pipeline (Anglada-Escudé & Butler 2012), and asymmetry indexes BIS, ΔV, and $V_{\rm asy}$ derived as described in Lanza et al. (2018). The RV errors reported are the formal ones, not including the jitter term. In Table A.2 we list the observation dates and the activity indexes Ca II H and K, Hα, Na I D_1 D_2, and He I D_3, derived following the procedure by Gomes da Silva et al. (2011).

Table A.1. RV and asymmetry indexes data of the 106 observed HARPS-N spectra of GJ 685.

BJD−2 400 000 (d)	RV ($m\,s^{-1}$)	RV_{Err} ($m\,s^{-1}$)	BIS	BIS_{Err}	ΔV	ΔV_{Err}	V_{asy}	$V_{asy,\,Err}$
56 439.6165	−3.74	0.83	0.0487	0.0068	0.060	0.019	−0.070	0.012
56 440.6070	−3.01	0.89	0.0423	0.0069	0.053	0.019	−0.057	0.012
56 443.4917	3.00	0.99	0.0401	0.0046	0.050	0.017	−0.061	0.012
56 443.7301	6.01	1.16	0.0396	0.0047	0.049	0.016	−0.061	0.012
56 444.5211	7.73	0.68	0.0416	0.0056	0.052	0.019	−0.060	0.012
56 454.6490	−3.00	0.60	0.0458	0.0069	0.056	0.018	−0.065	0.012
56 455.6660	−5.61	0.76	0.0458	0.0061	0.058	0.019	−0.067	0.012
56 483.5766	5.62	1.32	0.0286	0.0063	0.038	0.020	−0.038	0.013
56 484.5451	0.47	0.75	0.0465	0.0063	0.057	0.019	−0.067	0.012
56 485.5714	−5.93	0.69	0.0462	0.0063	0.056	0.018	−0.068	0.012
56 486.5469	−5.58	0.70	0.0483	0.0072	0.059	0.020	−0.066	0.012
56 487.5532	−2.26	0.90	0.0409	0.0063	0.052	0.019	−0.058	0.012
56 506.5333	−1.73	0.90	0.0398	0.0061	0.050	0.020	−0.051	0.012
56 533.3947	0.90	0.64	0.0412	0.0067	0.052	0.020	−0.055	0.012
56 534.4035	4.43	0.78	0.0409	0.0058	0.052	0.019	−0.057	0.012
56 534.5066	4.02	0.81	0.0440	0.0078	0.055	0.019	−0.061	0.013
56 535.3775	13.35	0.91	0.0434	0.0063	0.051	0.022	−0.057	0.012
56 536.5216	22.22	1.15	0.0372	0.0050	0.046	0.022	−0.060	0.013
56 537.4850	13.14	0.99	0.0322	0.0035	0.041	0.018	−0.051	0.012
56 693.7377	−12.55	0.89	0.0491	0.0070	0.064	0.018	−0.073	0.012
56 694.7625	−13.16	1.37	0.0456	0.0068	0.056	0.019	−0.063	0.013
56 695.7888	−3.93	1.03	0.0505	0.0056	0.060	0.020	−0.080	0.013
56 696.7350	−2.05	0.64	0.0404	0.0051	0.052	0.018	−0.061	0.013
56 697.7342	5.58	0.89	0.0429	0.0053	0.054	0.019	−0.064	0.012
56 698.7363	5.00	1.22	0.0379	0.0055	0.046	0.019	−0.050	0.012
56 699.6943	4.12	0.70	0.0425	0.0055	0.052	0.018	−0.062	0.012
56 700.7016	2.75	0.74	0.0489	0.0077	0.061	0.021	−0.066	0.012
56 701.7040	1.92	0.83	0.0504	0.0075	0.061	0.020	−0.069	0.012
56 702.7237	8.12	1.05	0.0468	0.0064	0.060	0.020	−0.074	0.013
56 786.5800	−2.18	0.90	0.0476	0.0082	0.058	0.020	−0.063	0.014
56 787.6315	1.84	1.31	0.0426	0.0070	0.056	0.019	−0.062	0.014
56 811.5545	−6.35	0.69	0.0423	0.0071	0.055	0.020	−0.059	0.013
56 854.5592	−0.73	0.73	0.0488	0.0082	0.062	0.020	−0.067	0.013
56 855.5368	−2.65	0.76	0.0507	0.0077	0.064	0.020	−0.073	0.013
57 069.7411	1.54	0.57	0.0467	0.0077	0.060	0.020	−0.067	0.014
57 070.7726	−3.18	1.20	0.0462	0.0069	0.055	0.019	−0.060	0.014
57 145.7379	−0.17	0.70	0.0429	0.0082	0.056	0.020	−0.058	0.014
57 148.6158	2.58	1.00	0.0433	0.0070	0.053	0.022	−0.058	0.013
57 170.5973	−5.50	0.72	0.0499	0.0061	0.064	0.018	−0.079	0.013
57 172.6445	−5.64	0.73	0.0513	0.0062	0.063	0.018	−0.078	0.013
57 209.5337	2.58	1.14	0.0437	0.0062	0.055	0.020	−0.064	0.014
57 289.3896	−1.81	1.18	0.0354	0.0063	0.047	0.018	−0.048	0.015
57 291.4060	4.80	0.82	0.0405	0.0056	0.050	0.020	−0.057	0.013
57 297.4116	1.51	1.64	0.0495	0.0062	0.058	0.023	−0.078	0.015
57 472.6602	−2.32	0.99	0.0573	0.0076	0.067	0.022	−0.082	0.014
57 474.6766	−0.08	0.82	0.0440	0.0059	0.057	0.021	−0.066	0.013
57 475.6565	5.07	1.25	0.0465	0.0087	0.056	0.024	−0.059	0.014
57 501.6422	−0.77	0.94	0.0519	0.0068	0.064	0.019	−0.079	0.013

Notes. We list observation epochs, RVs, BIS, ΔV, $V_{\rm asy}$, and the respective errors.

Table A.1. continued.

BJD−2 400 000 (d)	RV ($m\,s^{-1}$)	RV_{Err} ($m\,s^{-1}$)	BIS	BIS_{Err}	ΔV	ΔV_{Err}	V_{asy}	$V_{asy,\,Err}$
57 549.7017	7.38	1.33	0.0484	0.0063	0.062	0.027	−0.081	0.014
57 603.4803	8.16	0.83	0.0342	0.0053	0.045	0.019	−0.053	0.014
57 604.4710	3.38	1.01	0.0335	0.0048	0.045	0.019	−0.053	0.013
57 620.4417	8.48	1.23	0.0450	0.0068	0.055	0.021	−0.065	0.014
57 621.4791	6.49	3.74	0.0291	0.0134	0.041	0.021	−0.024	0.020
57 622.4623	10.05	0.98	0.0423	0.0048	0.053	0.018	−0.066	0.013
57 623.4452	4.67	1.11	0.0508	0.0078	0.061	0.021	−0.073	0.013
57 624.4137	4.62	0.77	0.0475	0.0060	0.056	0.022	−0.065	0.013
57 644.3556	3.10	1.11	0.0479	0.0058	0.060	0.019	−0.076	0.013
57 650.3812	3.38	0.93	0.0441	0.0051	0.052	0.018	−0.067	0.013
57 916.6963	−7.16	1.19	0.0496	0.0089	0.058	0.020	−0.065	0.014
57 928.6057	16.08	2.71	0.0330	0.0099	0.038	0.027	−0.056	0.017
57 930.5601	17.05	1.36	0.0397	0.0057	0.046	0.029	−0.067	0.015
57 932.5778	−2.89	0.81	0.0477	0.0073	0.059	0.018	−0.070	0.014
57 933.5794	−6.32	0.86	0.0432	0.0045	0.054	0.018	−0.067	0.013
57 934.5802	−6.24	0.93	0.0415	0.0061	0.054	0.019	−0.062	0.014
57 935.5355	−0.47	0.81	0.0481	0.0067	0.057	0.018	−0.071	0.014
57 936.5379	2.00	0.94	0.0491	0.0056	0.057	0.018	−0.074	0.014
57 937.6435	5.44	1.06	0.0462	0.0056	0.056	0.018	−0.070	0.013
57 942.6500	−8.47	0.76	0.0492	0.0069	0.058	0.020	−0.069	0.013
57 943.5814	−9.78	1.00	0.0461	0.0050	0.057	0.017	−0.073	0.013
57 944.4845	−2.17	0.71	0.0383	0.0052	0.049	0.018	−0.060	0.013
57 949.5628	−0.90	1.41	0.0319	0.0054	0.044	0.019	−0.046	0.014
57 950.5477	−9.01	1.24	0.0538	0.0055	0.065	0.018	−0.082	0.014
57 952.5300	−11.84	1.05	0.0552	0.0062	0.066	0.019	−0.083	0.013
57 953.4719	−8.35	0.93	0.0411	0.0068	0.053	0.018	−0.061	0.014
57 954.5128	−1.55	0.73	0.0455	0.0068	0.059	0.019	−0.071	0.014
57 956.4444	4.21	0.81	0.0404	0.0047	0.051	0.019	−0.061	0.013
57 961.4980	−2.13	0.97	0.0520	0.0066	0.064	0.019	−0.077	0.013
57 971.3955	−10.51	1.00	0.0434	0.0064	0.056	0.018	−0.064	0.013
57 972.4675	−7.03	1.04	0.0503	0.0064	0.060	0.018	−0.073	0.014
57 973.4635	−3.88	1.26	0.0495	0.0077	0.057	0.018	−0.072	0.015
57 974.4251	−4.79	1.13	0.0441	0.0070	0.054	0.019	−0.064	0.014
57 975.4988	0.00	1.03	0.0408	0.0053	0.050	0.018	−0.063	0.014
57 976.5033	1.99	1.05	0.0400	0.0056	0.052	0.018	−0.062	0.014
57 978.4249	−3.92	0.80	0.0458	0.0058	0.056	0.020	−0.067	0.013
57 980.4545	−0.57	0.86	0.0422	0.0063	0.052	0.021	−0.060	0.013
57 981.4380	3.02	0.64	0.0429	0.0064	0.054	0.020	−0.062	0.013
57 984.4839	8.01	0.91	0.0387	0.0059	0.046	0.019	−0.054	0.013
57 989.3821	−5.00	1.12	0.0352	0.0046	0.044	0.018	−0.051	0.014
57 991.3941	3.43	2.22	0.0317	0.0088	0.042	0.026	−0.052	0.017
57 992.3841	−1.75	1.03	0.0418	0.0051	0.050	0.019	−0.065	0.014
57 993.4441	0.71	2.14	0.0295	0.0098	0.038	0.019	−0.050	0.017
57 994.3785	1.43	0.97	0.0420	0.0058	0.050	0.020	−0.064	0.014
57 995.3651	4.59	0.97	0.0392	0.0043	0.048	0.020	−0.063	0.014
57 996.3687	−3.46	1.00	0.0367	0.0058	0.048	0.018	−0.056	0.014
57 997.4147	−3.41	0.73	0.0485	0.0070	0.061	0.018	−0.074	0.014
57 999.3666	1.15	1.01	0.0468	0.0065	0.058	0.018	−0.071	0.013
58 000.4202	6.53	1.27	0.0455	0.0072	0.051	0.018	−0.063	0.014
58 001.3637	6.19	1.37	0.0528	0.0082	0.058	0.019	−0.074	0.015
58 006.4189	−3.21	0.64	0.0438	0.0060	0.053	0.018	−0.063	0.014
58 008.4121	1.76	0.78	0.0481	0.0063	0.060	0.020	−0.070	0.013
58 010.3947	−0.78	0.95	0.0468	0.0067	0.059	0.019	−0.073	0.014
58 019.3429	5.08	1.76	0.0523	0.0072	0.063	0.019	−0.080	0.015
58 024.3564	−6.84	0.84	0.0434	0.0055	0.051	0.018	−0.064	0.013
58 026.3398	−0.24	0.90	0.0464	0.0067	0.057	0.019	−0.067	0.013
58 031.3905	0.18	0.96	0.0407	0.0055	0.050	0.018	−0.061	0.013
58 044.3502	−3.02	1.00	0.0411	0.0053	0.052	0.018	−0.062	0.014

Table A.2. Activity indexes data of the 106 observed HARPS-N spectra of GJ 685.

BJD−2 400 000	RV	RV_{Err}	BIS	BIS_{Err}	ΔV	ΔV_{Err}	V_{asy}	$V_{asy,\,Err}$
56 439.6165	0.09561	0.00064	0.062060	0.000107	0.004638	0.000023	0.04049	0.00013
56 440.6070	0.08841	0.00065	0.060442	0.000110	0.004583	0.000024	0.04043	0.00014
56 443.4917	0.08535	0.00092	0.059510	0.000147	0.004490	0.000033	0.03944	0.00020
56 443.7301	0.07298	0.00083	0.059985	0.000157	0.004671	0.000036	0.03949	0.00021
56 444.5211	0.08791	0.00062	0.060539	0.000110	0.004570	0.000023	0.03946	0.00013
56 454.6490	0.10000	0.00070	0.063561	0.000111	0.004716	0.000024	0.03960	0.00014
56 455.6660	0.10666	0.00082	0.065671	0.000129	0.004852	0.000027	0.04068	0.00016
56 483.5766	0.10201	0.00144	0.062962	0.000228	0.004861	0.000049	0.03965	0.00028
56 484.5451	0.10009	0.00075	0.062777	0.000118	0.004669	0.000025	0.03937	0.00015
56 485.5714	0.09804	0.00069	0.062531	0.000102	0.004577	0.000023	0.04056	0.00014
56 486.5469	0.09839	0.00066	0.063194	0.000114	0.004696	0.000024	0.04052	0.00014
56 487.5532	0.10118	0.00082	0.063952	0.000127	0.004697	0.000027	0.03950	0.00016
56 506.5333	0.10125	0.00086	0.063597	0.000147	0.004881	0.000031	0.03944	0.00017
56 533.3947	0.08336	0.00052	0.060286	0.000099	0.004542	0.000020	0.03930	0.00012
56 534.4035	0.08413	0.00072	0.060381	0.000130	0.004532	0.000027	0.03939	0.00016
56 534.5066	0.08706	0.00094	0.060720	0.000147	0.004551	0.000032	0.03936	0.00019
56 535.3775	0.09179	0.00072	0.062070	0.000141	0.004758	0.000028	0.04070	0.00016
56 536.5216	0.09398	0.00080	0.062810	0.000099	0.004211	0.000023	0.04024	0.00015
56 537.4850	0.10041	0.00074	0.063841	0.000108	0.004498	0.000024	0.03931	0.00014
56 693.7377	0.09503	0.00091	0.062017	0.000138	0.004724	0.000030	0.04078	0.00018
56 694.7625	0.08591	0.00087	0.059852	0.000137	0.004475	0.000031	0.04069	0.00019
56 695.7888	0.08653	0.00107	0.060192	0.000152	0.004313	0.000037	0.04175	0.00023
56 696.7350	0.08568	0.00088	0.061051	0.000138	0.004478	0.000031	0.04077	0.00019
56 697.7342	0.09726	0.00080	0.063246	0.000128	0.004833	0.000028	0.04118	0.00016
56 698.7363	0.08939	0.00096	0.061495	0.000154	0.004597	0.000034	0.04087	0.00020
56 699.6943	0.09492	0.00068	0.062424	0.000099	0.004566	0.000022	0.04067	0.00013
56 700.7016	0.09748	0.00070	0.063375	0.000118	0.004792	0.000024	0.04075	0.00014
56 701.7040	0.09479	0.00074	0.063197	0.000128	0.004800	0.000027	0.04074	0.00015
56 702.7237	0.11418	0.00093	0.066657	0.000113	0.004633	0.000027	0.04104	0.00016
56 786.5800	0.08328	0.00091	0.059716	0.000160	0.004532	0.000034	0.04068	0.00020
56 787.6315	0.09222	0.00130	0.061135	0.000202	0.004665	0.000045	0.03936	0.00026
56 811.5545	0.09430	0.00076	0.061798	0.000121	0.004695	0.000027	0.04055	0.00016
56 854.5592	0.09375	0.00066	0.061102	0.000109	0.004712	0.000024	0.03958	0.00014
56 855.5368	0.08779	0.00060	0.060005	0.000102	0.004647	0.000022	0.04046	0.00013
57 069.7411	0.08977	0.00110	0.061213	0.000173	0.004606	0.000038	0.04046	0.00023
57 070.7726	0.08571	0.00127	0.060933	0.000184	0.004502	0.000043	0.04093	0.00026
57 145.7379	0.08263	0.00068	0.060525	0.000123	0.004541	0.000026	0.04067	0.00016
57 148.6158	0.08624	0.00074	0.061605	0.000137	0.004673	0.000029	0.04053	0.00017
57 170.5973	0.09509	0.00070	0.062790	0.000103	0.004510	0.000024	0.04050	0.00014
57 172.6445	0.09365	0.00083	0.061914	0.000115	0.004510	0.000027	0.04051	0.00016
57 209.5337	0.09108	0.00105	0.062632	0.000163	0.004586	0.000036	0.03964	0.00021
57 289.3896	0.07381	0.00106	0.058912	0.000189	0.004641	0.000044	0.03942	0.00025
57 291.4060	0.08401	0.00064	0.061866	0.000114	0.004513	0.000024	0.03951	0.00014
57 297.4116	0.09814	0.00156	0.061781	0.000172	0.004439	0.000046	0.03952	0.00029
57 472.6602	0.08774	0.00103	0.060410	0.000181	0.004625	0.000040	0.04072	0.00023
57 474.6766	0.08848	0.00072	0.061243	0.000131	0.004573	0.000028	0.04046	0.00016
57 475.6565	0.08742	0.00101	0.060990	0.000194	0.004677	0.000042	0.04057	0.00024
57 501.6422	0.10231	0.00121	0.063452	0.000173	0.004777	0.000040	0.04057	0.00023
57 549.7017	0.09461	0.00118	0.061545	0.000127	0.004290	0.000035	0.03937	0.00022
57 603.4803	0.10459	0.00082	0.063254	0.000107	0.004632	0.000026	0.03967	0.00016
57 604.4710	0.09771	0.00114	0.062192	0.000169	0.004651	0.000039	0.03966	0.00023
57 620.4417	0.09116	0.00097	0.061652	0.000164	0.004689	0.000037	0.03947	0.00021
57 621.4791	0.08421	0.00227	0.062241	0.000379	0.004968	0.000094	0.04003	0.00054
57 622.4623	0.09905	0.00096	0.063066	0.000138	0.004692	0.000033	0.03963	0.00019
57 623.4452	0.09386	0.00090	0.061852	0.000149	0.004709	0.000033	0.03943	0.00019
57 624.4137	0.09613	0.00072	0.062649	0.000132	0.004748	0.000028	0.03951	0.00016
57 644.3556	0.10144	0.00088	0.064186	0.000127	0.004679	0.000030	0.03938	0.00017
57 650.3812	0.09179	0.00088	0.061558	0.000141	0.004621	0.000032	0.03931	0.00019

Notes. We list observation epochs, Ca II H & K, Hα, Na I D_1 D_2, He I D_3, and the respective errors.

Table A.2. continued.

BJD−2 400 000	RV	RV_{Err}	BIS	BIS_{Err}	ΔV	ΔV_{Err}	V_{asy}	$V_{asy,\,Err}$
57 916.6963	0.08727	0.00108	0.061088	0.000189	0.004673	0.000042	0.04070	0.00025
57 928.6057	0.09166	0.00203	0.061891	0.000247	0.004639	0.000071	0.03970	0.00044
57 930.5601	0.10249	0.00145	0.063463	0.000152	0.004185	0.000042	0.03944	0.00027
57 932.5778	0.10408	0.00086	0.064630	0.000124	0.004626	0.000029	0.04090	0.00017
57 933.5794	0.09838	0.00090	0.062950	0.000140	0.004594	0.000032	0.04050	0.00019
57 934.5802	0.09272	0.00083	0.061708	0.000126	0.004505	0.000029	0.04068	0.00018
57 935.5355	0.10477	0.00086	0.065083	0.000131	0.004722	0.000030	0.04005	0.00017
57 936.5379	0.09064	0.00106	0.061315	0.000170	0.004571	0.000039	0.03958	0.00023
57 937.6435	0.08851	0.00086	0.060725	0.000130	0.004482	0.000030	0.03937	0.00018
57 942.6500	0.08518	0.00069	0.059722	0.000123	0.004565	0.000027	0.04048	0.00016
57 943.5814	0.10073	0.00117	0.063162	0.000164	0.004672	0.000039	0.04089	0.00023
57 944.4845	0.08810	0.00071	0.060404	0.000106	0.004416	0.000025	0.04054	0.00016
57 949.5628	0.09540	0.00125	0.062328	0.000190	0.004593	0.000044	0.04051	0.00026
57 950.5477	0.09760	0.00119	0.063236	0.000182	0.004748	0.000042	0.04075	0.00025
57 952.5300	0.09161	0.00088	0.061863	0.000143	0.004535	0.000032	0.04044	0.00019
57 953.4719	0.09659	0.00072	0.062843	0.000108	0.004568	0.000025	0.04081	0.00015
57 954.5128	0.08800	0.00072	0.060700	0.000101	0.004338	0.000024	0.03958	0.00015
57 956.4444	0.08439	0.00059	0.059468	0.000104	0.004498	0.000023	0.03920	0.00014
57 961.4980	0.08618	0.00082	0.060867	0.000146	0.004370	0.000031	0.04045	0.00019
57 971.3955	0.09186	0.00083	0.061743	0.000131	0.004540	0.000030	0.04079	0.00018
57 972.4675	0.09107	0.00102	0.062423	0.000167	0.004606	0.000038	0.04055	0.00022
57 973.4635	0.08250	0.00121	0.061649	0.000213	0.004824	0.000050	0.04043	0.00029
57 974.4251	0.08740	0.00100	0.061335	0.000171	0.004515	0.000038	0.04015	0.00023
57 975.4988	0.08835	0.00093	0.060880	0.000141	0.004418	0.000033	0.03929	0.00020
57 976.5033	0.08611	0.00096	0.060881	0.000148	0.004467	0.000035	0.03961	0.00021
57 978.4249	0.08847	0.00068	0.061783	0.000125	0.004615	0.000027	0.04068	0.00016
57 980.4545	0.08628	0.00063	0.060469	0.000121	0.004645	0.000026	0.04056	0.00015
57 981.4380	0.08487	0.00077	0.060199	0.000138	0.004595	0.000030	0.03925	0.00018
57 984.4839	0.10293	0.00085	0.064985	0.000137	0.004723	0.000030	0.03975	0.00018
57 989.3821	0.09273	0.00101	0.062176	0.000165	0.004556	0.000037	0.04026	0.00022
57 991.3941	0.09078	0.00185	0.061146	0.000221	0.004411	0.000063	0.04009	0.00040
57 992.3841	0.08631	0.00087	0.060948	0.000122	0.004271	0.000030	0.03944	0.00019
57 993.4441	0.08007	0.00175	0.061598	0.000273	0.005230	0.000072	0.03904	0.00040
57 994.3785	0.08639	0.00077	0.060204	0.000108	0.004301	0.000027	0.03949	0.00017
57 995.3651	0.09490	0.00092	0.062171	0.000118	0.004440	0.000030	0.03983	0.00019
57 996.3687	0.08769	0.00096	0.060458	0.000142	0.004428	0.000034	0.03922	0.00021
57 997.4147	0.08839	0.00088	0.060663	0.000126	0.004360	0.000030	0.04072	0.00019
57 999.3666	0.08730	0.00090	0.060661	0.000151	0.004488	0.000034	0.03952	0.00020
58 000.4202	0.09153	0.00115	0.061780	0.000176	0.004515	0.000041	0.03945	0.00024
58 001.3637	0.09534	0.00161	0.061638	0.000243	0.004416	0.000055	0.03933	0.00033
58 006.4189	0.09205	0.00077	0.062493	0.000121	0.004468	0.000028	0.04040	0.00017
58 008.4121	0.09355	0.00062	0.062458	0.000111	0.004563	0.000024	0.03939	0.00014
58 010.3947	0.09050	0.00092	0.061448	0.000153	0.004641	0.000035	0.04082	0.00021
58 019.3429	0.09684	0.00159	0.064748	0.000237	0.004888	0.000057	0.03995	0.00033
58 024.3564	0.09561	0.00066	0.062890	0.000106	0.004543	0.000024	0.04071	0.00014
58 026.3398	0.09090	0.00071	0.061864	0.000127	0.004599	0.000028	0.03958	0.00016
58 031.3905	0.08632	0.00077	0.061013	0.000126	0.004507	0.000029	0.03947	0.00017
58 044.3502	0.08742	0.00077	0.061133	0.000129	0.004492	0.000029	0.04058	0.00017